frontiers | Frontiers in Earth Science

ORIGINAL RESEARCH
published: 13 June 2022
doi: 10.3389/feart.2022.849665

Discovery of the Late Jurassic-Early Cretaceous Lamprophyres in Western Songliao Basin of Northeast China and Their Constraint on Regional Lithospheric Evolution

Taiji Yu[1], *Pujun Wang*[1]*, *Yan Zhang*[1], *Youfeng Gao*[1,2] *and Chongyang Chen*[3]

[1]College of Earth Sciences, Jilin University, Changchun, China, [2]Research Center of Palaeontology and Stratigraphy, Jilin University, Changchun, China, [3]College of Tourism and Geographic Sciences, Jilin Normal University, Siping, China

OPEN ACCESS

Edited by:
Kit Lai,
Fortescue Metals Group, Australia

Reviewed by:
Rui Wang,
China University of Geosciences, China
Chuan-Zhou Liu,
Institute of Geology and Geophysics (CAS), China

***Correspondence:**
Pujun Wang
wangpj@jlu.edu.cn

Specialty section:
This article was submitted to Petrology, a section of the journal Frontiers in Earth Science

Received: *06 January 2022*
Accepted: *18 May 2022*
Published: *13 June 2022*

Citation:
Yu T, Wang P, Zhang Y, Gao Y and Chen C (2022) Discovery of the Late Jurassic-Early Cretaceous Lamprophyres in Western Songliao Basin of Northeast China and Their Constraint on Regional Lithospheric Evolution. Front. Earth Sci. 10:849665. doi: 10.3389/feart.2022.849665

Contrary to the commonly accepted notion that the lithosphere in NE China thinned from the Late Jurassic through to the Early Cretaceous period, we report the discovery of a thickening episode in the backdrop of this long-term thinning. A series of lamprophyre dikes have been recently discovered in the Tuquan Basin of the western Songliao Basin that have been dated to 156.0 ± 2.3 Ma, 132.9 ± 1.2 Ma, and 126.2 ± 2.5 Ma by using the zircon U–Pb technique. These lamprophyres are subdivided into biotite orthoclase lamprophyre (BOL) from the Late Jurassic and quartz magnetite lamprophyre (QML) from the Early Cretaceous. The BOL and QMLs are shoshonite and calc-alkaline in series, are characterized by large amounts of FeO^T, TiO_2, MgO, and Mg#, and are rich in LREEs and LILEs but poor in HREEs and HFSEs. They have high ratios of $(La/Yb)_N$, La/Ta, La/Nb, Th/Y, Ba/Nb, Ba/Ta, and Ba/Th, and low ratios of Zr/Ba, La/Sm, and Nb/Zr. These features collectively point to the derivation of dike magmas from the partial melting of the enriched lithospheric mantle that had been previously metasomatized by subduction-related fluids. The BOL has high ratios of Rb/Sr (0.42) and K/Yb*1000 (28.3), and low ratios of Ba/Rb (13.5) and Dy/Yb (2.35), suggesting the derivation of magma from a high degree of partial melting of the phlogopite-bearing lherzolite mantle in the spinel–garnet transition zone at a depth of about 60 km. The QMLs have low ratios of Rb/Sr (0.02–0.06) and K/Yb*1000 (8.13–19.73), and high ratios of Ba/Rb (17.6–42.6) and Dy/Yb (3.48–4.09), indicating that the magmas were derived from a low degree of partial melting of the lherzolite mantle in the garnet zone at a depth of ca. 85 km. The younger QML (126.2 ± 2.5 Ma) has a lower Dy/Yb ratio (3.48–3.92) than the older QML (132.9 ± 1.2 Ma), with a Dy/Yb ratio of 4.09 implying that the younger magma was formed at a shallower depth of the mantle (<85 km) than the older one. These observations indicate that in 156–132 Ma, the lithosphere thickened by approximately 25 km at a rate of approximately 1.0 km/Myr. This is used to propose a model of geodynamic evolution in three stages.

Keywords: Songliao Basin, Northeast Asia, lamprophyre, geochemistry, lithospheric evolution, Jurassic and Cretaceous

1 INTRODUCTION

Lamprophyres are alkaline/calc-alkaline, mafic, or ultramafic melanocratic hypabyssal igneous rocks characterized by porphyritic textures, with mafic phenocrysts (biotite and/or amphibole) and groundmass mainly consisting of alkali feldspar, plagioclase, feldspathoids, biotite, amphibole, clinopyroxene, and olivine (Rock, 1991). They often occur as dikes (Le Maitre, 2002). Based on the type and content of feldspar and predominant mafic minerals in them, lamprophyres can be categorized into minette, spessartite, and sannaite (Le Maitre, 2002). Distributed widely across the globe, lamprophyres were formed in the Archean (Wyman et al., 2006), the Paleozoic (Rocchi et al., 2009), the Mesozoic (Deng et al., 2017) and the Cenozoic (Li et al., 2002). Lamprophyric magmas are generally thought to have originated from the partial melting of an enriched continental lithospheric mantle (Rock, 1987; Gibson et al., 2006; Choi et al., 2020). Their capacity to record the material composition of the deep lithospheric mantle, mantle–crust interactions, and the process of enrichment of the lithospheric mantle makes lamprophyres an important means of studying the evolution of the continental lithosphere (Rock and Groves, 1988; Stille et al., 1989). Most lamprophyres were formed in extensional tectonic settings (Woolley et al., 1996; Secher et al., 2009) while some have also been identified in convergent settings (Owen, 2008; van der Meer et al., 2016). Lamprophyres are commonly found in collisional orogens, such as southern Tibet and the Sanjiang Belt (Chung et al., 2005; Ding et al., 2007). The mineral and geochemical features of lamprophyres are vital for investigating the properties of the continental lithospheric mantle (Foley et al., 1987; Soder and Romer, 2018) and dynamic processes in the deep Earth (Guo et al., 2004; Ma et al., 2014; Deng et al., 2017).

It is widely believed that the lithosphere in northeast (NE) China thinned significantly from the Late Jurassic through the Early Cretaceous period (Wang et al., 2006; Wu et al., 2011; Zhang et al., 2011). Delamination is the main mechanism of lithospheric thinning (Zhang et al., 2010). However, there are differences in the estimated periods of lithospheric thinning. The estimates include 160–120 Ma (Wang et al., 2006), 162–125 Ma (Zhang et al., 2020), 155–123 Ma (Tang et al., 2015), 136–109 Ma (Zhang et al., 2011), and 135–90 Ma (Ji et al., 2021). Whether thickening occurred during the long period of lithospheric thinning from 162 to 90 Ma, and what the rates of thinning and/or thickening are outstanding questions.

Geodynamic models of lithospheric thinning include the subduction and suture of the Mongol–Okhotsk Ocean from the west (Wang et al., 2006), and the subduction of the Paleo-Pacific Plate from the east (Zhang et al., 2010; Zhang et al., 2011). It is generally recognized that the Mongol–Okhotsk tectonic regime ranges from the Siberian craton in the northwest to the Erguna–Xing'an–Songliao Blocks in the southeast (Tang et al., 2015; Li et al., 2018; Zhang et al., 2020), whereas the Paleo-Pacific tectonic domain ranges from Jiamusi Block in the southeast to the Songliao Block (Zhang et al., 2010; Guo et al., 2015; Wang et al., 2019), and even to the Erguna Block (Ji et al., 2021) in the northwest. This means that the lithospheric thinning and/or thickening of the Songliao Basin and the Great Xing'an Range during 162–90 Ma may have been influenced by the two-sided geodynamics of both the Mongol–Okhotsk Ocean from the west and the Paleo-Pacific Plate from the east. This raises the challenge of identifying the dominant geodynamic factor in a given period in this region that led to the lithospheric changes.

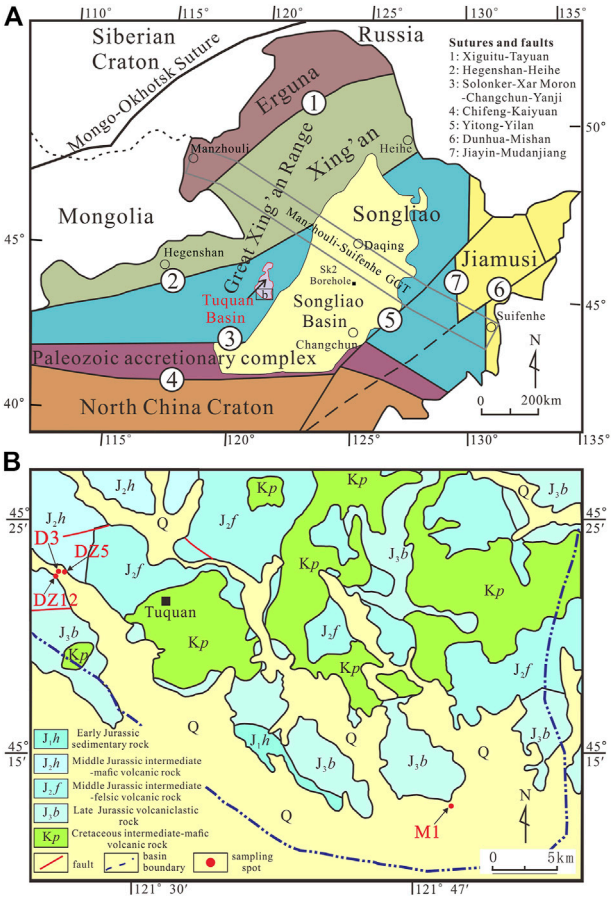

FIGURE 1 | (A) Tectonic subdivisions of northeastern China and the location of the Tuquan Basin (modified after Wu et al., 2011). GGT indicates Global Geosciences Transect. **(B)** Simplified geological map of the Tuquan Basin showing sample locations modified after Inner Jilin Bureau of Geology and Mineral Resources (1977).

We have discovered two types of lamprophyre intrusions—the biotite orthoclase lamprophyre (BOL) and the quartz magnetite lamprophyre (QML)—in the Tuquan Basin along the western margin of the Songliao Basin in northeast China. The BOL showed zircon U–Pb isotopic ages of 156.0 ± 2.3 Ma, whereas the QMLs showed zircon U–Pb isotopic ages of 132.9 ± 1.2 Ma and 126.2 ± 2.5 Ma. The petrologic and geochemical results presented in this paper indicate that the lamprophyres with these three ages recorded three different lithospheric thicknesses and corresponding geodynamic processes. They provide a reasonable constraint on the time limits of the Mongol–Okhotsk oceanic subduction, continental collision, and post-collisional extension, from the Siberian Craton via the Mongol–Okhotsk Suture Zone to the Songliao Block during the Late Jurassic through to the Early Cretaceous.

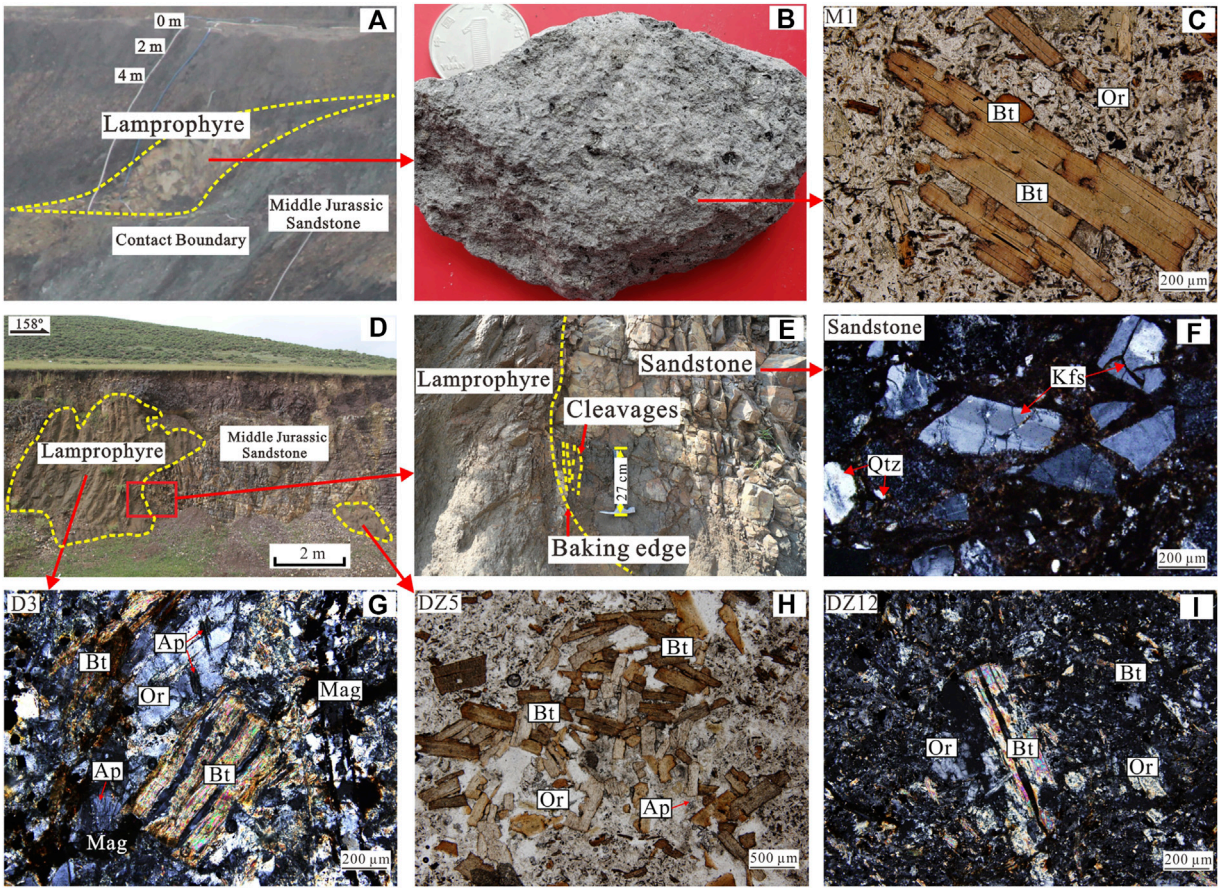

FIGURE 2 | Lamprophyre dikes of the Late Jurassic and the Early Cretaceous intruded in the Middle Jurassic sedimentary sequences. **(A,D)** Photographs of the lamprophyre dikes intruded into the Jurassic sandstone; **(B)** Photograph of the lamprophyre specimen; **(C)** Micro photograph of the Jurassic lamprophyre with typical lamprophyric texture, mainly composed of biotite and orthoclase (named as BOL in this paper); **(E)** The contact between the lamprophyre and the surrounding rock; **(F)** Micro photograph of the Jurassic sandstone intruded by lamprophyres, mainly composed of quartz and feldspar; **(G–I)** Micro photographs of the Cretaceous lamprophyres with typical lamprophyric texture, mainly composed of biotite, orthoclase, magnetite, apatite, and tiny quartz crystals (named as QMLs in this paper). Bt, biotite; Or, orthoclase; Ap, apatite; Mag, magnetite; Pl, plagioclase; Qtz, quartz; Kfs, k-feldspar.

2 GEOLOGICAL SETTINGS AND DESCRIPTION OF SAMPLES

The tectonic components of NE China include the Erguna Block, the Xing'an Block, the Songliao Block, and the Jiamusi Block (from NW to SE). They are separated by suture zones of Xiguitu–Tayuan, Hegenshan–Heihe, and Jiayin–Mudanjiang, respectively (**Figure 1A**; Wu et al., 2011; Liu et al., 2017). The Tuquan Basin of the study area is along the western margin of the Songliao Basin (**Figure 1A**). The outcropping strata in the Tuquan Basin are composed primarily of Jurassic sedimentary rocks and volcanic rocks that were intruded by mafic and intermediate dikes of the Late Jurassic and the Early Cretaceous. The lamprophyre samples examined (M1, D3, DZ5, and DZ12) appeared as a series of small and densely spaced intrusions into the sedimentary sequences from the Middle Jurassic (**Figure 1B**). Appearing in the form of dikes with thicknesses of approximately 2–6 m, the lamprophyres are generally distributed northeast in terms of orientation, with clear contact boundaries with the surrounding Jurassic sandstones (**Figures 2A,D**) that had been baked and cleaved at the contact surface between the lamprophyres and the surrounding rocks (**Figures 2E,F**). All the studied samples, numbered M1, D3, DZ5, and DZ12, were categorized as minette, a type of lamprophyre abundant in biotite and orthoclase, as described in Table 2.9 by Le Maitre (2002). **Table 1** summarizes their mineral composition and characteristics under a microscope, as shown in **Figure 2**.

3 ANALYTICAL METHODS

3.1 Zircon U–Pb Dating

Zircon crystals were extracted from whole-rock samples by combining magnetic and heavy liquid separation, and then handpicking them under a binocular microscope at the Langfang Regional Geological Survey in Hebei Province of China. All zircons were examined under transmitted and

TABLE 1 | Mineral composition and characteristics of lamprophyres under microscope.

Minerals	BOL (M1)			QMLs (D3, DZ5, and DZ12)		
	Content (%)	Grain size (mm)	Characteristic	Content (%)	Grain size (mm)	Characteristic
Biotite	60	0.10–1.50	Lam; Aci	40–50	0.10–1.10	Lam; Cru
Orthoclase	40	0.06–0.12	Mcr	25–35	0.01–0.63	Mcr; Ccr
Magnetite	<1	0.02–0.10	Mgr	10–30	0.02–0.30	Mgr; DDS
Apatite	<1	0.02–0.09	Aci	5	0.01–0.24	Aci; Col
Quartz	None	None	None	<1	0.01–0.05	Ccr; Mcr
Zircon	24 grain/kg	0.06–0.17	Mcr; Col	(34–40) grain/kg	0.05–0.13	Mcr; Col

Lam, lamellar; Aci, acicular; Col, columnar; Ccr, cryptocrystalline; Mcr, microcrystalline; Mgr, microgranular; Cru, crumpled; DDS, dense disseminated structure. Content (%) is area percentage.

reflected light micrographs with an optical microscope. To identify their internal structures, cathodoluminescence (CL) images were obtained using a JEOL scanning electron microscope. Grains of transparent, euhedral, unfractured, and inclusion-free zircons were chosen for isotopic analyses.

Zircon U–Pb analyses with a laser ablation–inductively coupled plasma mass spectrometer (LA–ICP–MS) were performed using an Agilent 7500a ICP–MS equipped with a 193-nm laser at the State Key Laboratory of Geological Processes and Mineral Resources, China University of Geosciences, Wuhan. Zircon 91500 was used as an external standard for age calibration, and NIST SRM 610 silicate glass was applied for instrument optimization. The diameter of the crater was 32 μm during the analyses. The parameters of the instrument and detailed procedures of their use have been described by Yuan et al. (2004). ICPMSDataCal (Ver. 6.7; Liu et al., 2010) and Isoplot (Ver. 3.0; Ludwig, 2003) were used for data reduction. Corrections were made for common Pb following Andersen (2002). Errors in individual LA–ICP–MS analyses were quoted at the 1σ level while errors in the pooled ages were quoted at a 95% (2σ) confidence level.

3.2 Geochemistry of Major and Trace Elements

Samples for geochemical analysis were crushed in an agate mill to a ~200 mesh after the removal of the altered surfaces. The major and trace element concentrations of the lamprophyre samples were determined at the Key Laboratory of Mineral Resources Evaluation in Northeast Asia (Ministry of National Resources of the People's Republic of China, Jilin University, Changchun, China). The major elements were analyzed using X-ray fluorescence (XRF; Rigaku ZSX Primu II) and fused glass disks. We determined the FeO content and the loss on ignition (LOI) values by volumetric and gravimetric methods, respectively. The trace elements were analyzed by using an Agilent 7500a ICP–MS, once the sample powders had been dissolved at high pressure in Teflon bombs. The analytical precisions of identification of the major and trace elements were higher than 1% and 5%, respectively, as determined by repeated analyses according to the USGS BHVO-1, BCR-2, and AGV-1 standards (Rudnick et al., 2004).

4 RESULTS

4.1 Zircon Characteristics and U–Pb Geochronology

Three lamprophyre samples (i.e., M1, D3, and DZ5) were each subjected to a zircon U–Pb dating analysis by using LA–ICP–MS. Colorless and transparent zircon crystals were selected for analysis. Consisting primarily of long and short columnar grains with diameters of 87–142 μm and length/width ratios of 1: 1–3: 1, the zircons displayed a relatively intact morphology with discernible edges and corners, and contained clear oscillatory zones along the edges. With a Th/U ratio greater than 0.2, the zircons were magmatic in origin (Hoskin and Schaltegger, 2003). Samples M1, D3, and DZ5 with older zircons also contained oscillatory growth zoning that was visible in CL imaging, and had Th/U values of 0.20–1.43, indicating that these zircons also had magmatic origins. They were likely to be inherited zircons derived from the subducted crust in the mantle source (Tarney and Jones, 1994). The results of dating are presented in **Table 2**.

A total of 25 zircons retrieved from sample M1 were dated using the U–Pb technique. The results (as shown in **Figure 3A**; **Table 2**) revealed relatively concordant $^{206}Pb/^{238}U$ and $^{207}Pb/^{235}U$ ratios, suggesting that the U–Pb system in the zircons had remained in a closed state and had not lost Pb after formation. Nine of the test points were concentrated near the age of 156 Ma. The $^{206}Pb/^{238}U$–$^{207}Pb/^{235}U$ concordia diagram yielded a concordant age of 156.0 ± 2.3 Ma (mean-squared weighted deviation (MSWD) = 2.1), representing the age of crystallization of the lamprophyre. In other words, the lamprophyre was formed in the Late Jurassic. The other 16 relatively old zircons were likely to have been inherited zircons within the sample.

A total of 27 zircons were tested for sample D3. The results (**Figure 3B**; **Table 2**) revealed relatively concordant $^{206}Pb/^{238}U$ and $^{207}Pb/^{235}U$ ratios, suggesting that the U–Pb system in the zircons had remained in a closed state and had not lost Pb after formation. Specifically, 13 test points were concentrated near 133 Ma. The $^{206}Pb/^{238}U$–$^{207}Pb/^{235}U$ concordia diagram yielded a concordant age of 132.9 ± 1.2 Ma (MSWD = 1.2), representing the age of crystallization of the lamprophyre and indicating that it had been formed in the Early Cretaceous. The other 14 relatively old zircons were likely to have been inherited zircons within the sample.

TABLE 2 | LA–ICP–MS U–Pb isotopic data for zircons from the lamprophyres in the Tuquan Basin.

Spot	Th/U	Contents ($\times10^{-6}$)			$^{207}Pb/^{206}Pb$		$^{207}Pb/^{235}U$		$^{206}Pb/^{238}U$		$^{207}Pb/^{206}Pb$		$^{207}Pb/^{235}U$		$^{206}Pb/^{238}U$	
		Pb	Th	U	Ratio	1σ	Ratio	1σ	Ratio	1σ	Age (Ma)	1σ	Age (Ma)	1σ	Age (Ma)	1σ
M1																
M1-1	0.70	20.26	130.28	186.31	0.051	0.0032	0.2062	0.0113	0.0301	0.0004	238.96	150.91	190.35	9.52	191.32	2.78
M1-2	0.65	11.98	73.19	111.98	0.0516	0.0033	0.2327	0.0133	0.0333	0.0006	333.39	143.50	212.46	10.92	211.42	3.63
M1-3	0.61	16.70	115.18	188.85	0.1187	0.0774	0.1736	0.024	0.0264	0.0006	1936.73	857.41	162.52	20.74	167.85	4.00
M1-4	0.35	11.08	71.96	207.11	0.0485	0.0026	0.1626	0.0081	0.0247	0.0004	120.46	122.20	152.96	7.09	157.16	2.44
M1-5	0.61	36.62	293.88	482.57	0.0501	0.0024	0.1655	0.0078	0.0242	0.0003	198.23	111.10	155.47	6.78	153.99	1.75
M1-6	0.56	22.84	163.89	293.33	0.0488	0.0023	0.1613	0.007	0.0243	0.0003	200.08	111.10	151.88	6.11	154.63	1.95
M1-7	1.12	50.32	170.89	153.26	0.0579	0.0033	0.4795	0.0278	0.0597	0.0007	524.11	130.54	397.71	19.05	373.67	4.29
M1-8	0.43	32.25	147.70	345.18	0.0515	0.0021	0.2496	0.0102	0.0351	0.0004	261.18	94.43	226.27	8.29	222.60	2.43
M1-9	0.37	2.02	10.82	29.02	0.0565	0.0087	0.1805	0.0256	0.0263	0.0009	472.27	347.02	168.53	22.01	167.50	5.78
M1-10	0.40	36.37	245.73	619.08	0.0499	0.0026	0.1639	0.0068	0.0244	0.0003	190.82	120.35	154.09	5.96	155.39	1.92
M1-11	0.20	30.25	108.94	553.56	0.0499	0.0019	0.2273	0.0093	0.0334	0.0007	190.82	88.88	208.01	7.70	211.79	4.38
M1-12	0.53	43.69	154.42	294.10	0.0529	0.0018	0.3632	0.0122	0.0499	0.0005	324.13	112.03	314.58	9.08	314.00	2.92
M1-13	0.03	9.08	11.86	421.22	0.0493	0.002	0.1859	0.0072	0.0275	0.0003	161.20	94.43	173.13	6.17	174.58	1.74
M1-14	0.43	110.24	472.25	1091.46	0.0509	0.0012	0.2764	0.0065	0.0393	0.0003	235.25	55.55	247.78	5.16	248.62	1.97
M1-15	0.53	17.03	131.87	250.79	0.0504	0.0029	0.1651	0.0085	0.0244	0.0004	213.04	131.46	155.14	7.40	155.48	2.25
M1-16	0.54	53.87	161.27	297.57	0.0486	0.0021	0.3256	0.015	0.0481	0.0005	127.87	103.69	286.20	11.48	303.11	3.21
M1-17	0.08	20.07	21.90	278.04	0.0134	0.0183	0.1709	0.0539	0.0251	0.0006	none	none	160.24	46.72	160.11	3.55
M1-18	0.83	91.92	244.21	294.54	0.0546	0.0021	0.5186	0.0188	0.0693	0.0007	394.50	87.03	424.25	12.61	432.21	4.04
M1-19	0.70	27.23	131.36	188.10	0.0524	0.0032	0.3001	0.0175	0.0421	0.0005	301.91	134.24	266.48	13.64	265.63	3.27
M1-20	0.37	29.39	128.96	344.69	0.0513	0.002	0.2565	0.0098	0.0365	0.0003	253.77	90.73	231.85	7.93	230.82	2.16
M1-21	0.60	31.46	133.65	222.80	0.0524	0.0023	0.3056	0.0129	0.0425	0.0004	305.62	127.76	270.80	10.05	268.31	2.76
M1-22	0.24	45.94	261.22	1097.77	0.0489	0.0014	0.1647	0.0047	0.0244	0.0002	146.38	68.51	154.84	4.09	155.42	1.30
M1-23	0.83	156.76	447.72	539.76	0.0552	0.0012	0.5363	0.012	0.0703	0.0006	420.42	54.63	436.01	7.93	438.24	3.54
M1-24	0.68	28.13	162.39	237.90	0.051	0.0026	0.2347	0.0121	0.0337	0.0005	238.96	118.50	214.08	9.96	213.90	3.40
M1-25	0.51	101.79	452.60	895.04	0.0884	0.0033	0.328	0.0099	0.0273	0.0004	1391.67	70.84	288.00	7.56	173.49	2.37
D3																
D3-1	0.86	68.63	636.62	757.93	0.0528	0.0019	0.156	0.0054	0.0213	0.0002	320.43	79.62	147.20	4.77	135.99	1.43
D3-2	0.37	3.52	33.65	90.23	0.0507	0.0058	0.1385	0.0131	0.0208	0.0005	233.40	244.42	131.72	11.64	133.02	3.24
D3-3	0.65	57.30	541.00	835.28	0.0494	0.0019	0.1379	0.0052	0.0203	0.0002	168.60	88.88	131.16	4.66	129.86	1.22
D3-4	0.73	25.46	232.75	335.33	0.0495	0.0025	0.1381	0.0064	0.0207	0.0003	172.31	115.73	131.32	5.73	131.97	1.66
D3-5	0.60	10.89	92.41	150.49	0.0506	0.0039	0.146	0.0093	0.0211	0.0004	220.44	179.61	138.34	8.20	134.56	2.24
D3-6	0.82	26.21	125.94	156.67	0.0571	0.0033	0.3116	0.0167	0.0399	0.0006	494.49	127.76	275.39	12.90	252.40	3.59
D3-7	0.47	21.20	131.67	282.82	0.0502	0.0024	0.1742	0.0073	0.0255	0.0003	205.63	104.62	163.06	6.31	162.02	2.08
D3-8	0.80	45.72	226.71	282.10	0.0521	0.0021	0.2821	0.0109	0.0396	0.0005	287.10	90.73	252.34	8.66	250.14	2.93
D3-9	0.63	30.40	145.84	230.39	0.0513	0.0024	0.2731	0.0121	0.0391	0.0005	253.77	109.24	245.20	9.62	247.35	2.86
D3-10	0.83	16.31	108.60	129.38	0.0515	0.0035	0.2023	0.0121	0.0292	0.0005	264.88	155.54	187.06	10.20	185.74	3.21
D3-11	0.38	65.39	273.01	601.07	0.0523	0.0049	0.2642	0.024	0.0395	0.001	298.21	208.31	238.03	19.25	250.03	6.46
D3-12	0.52	16.43	143.41	279.15	0.0499	0.0024	0.1435	0.0065	0.0209	0.0003	190.82	112.95	136.20	5.81	133.59	1.73
D3-13	0.41	9.36	73.33	176.07	0.0493	0.0032	0.1428	0.0085	0.0213	0.0003	161.20	148.13	135.51	7.52	135.64	2.18
D3-14	0.27	30.92	42.28	158.59	0.0607	0.002	0.8199	0.0266	0.098	0.001	627.80	72.21	607.97	14.85	602.75	5.77
D3-15	0.56	34.04	287.91	514.18	0.05	0.0022	0.1428	0.0058	0.0208	0.0002	194.53	99.99	135.52	5.19	132.87	1.45
D3-16	0.28	29.39	154.73	544.91	0.0499	0.0025	0.1845	0.009	0.0268	0.0003	190.82	113.87	171.90	7.72	170.65	2.02
D3-17	0.64	22.49	202.78	316.11	0.0487	0.0031	0.1408	0.0089	0.0209	0.0003	200.08	79.62	133.74	7.93	133.30	1.82
D3-18	0.75	24.95	125.97	177.65	0.0518	0.0027	0.2705	0.0133	0.0375	0.0005	275.99	120.35	243.08	10.67	237.20	2.90
D3-19	0.45	12.68	102.84	225.08	0.0495	0.0034	0.1392	0.0086	0.0206	0.0003	168.60	155.53	132.36	7.68	131.73	1.96
D3-20	0.45	35.01	103.41	260.37	0.0555	0.0022	0.4129	0.0157	0.0538	0.0006	435.23	88.88	350.96	11.30	338.11	3.58
D3-21	1.13	109.12	359.28	317.72	0.0624	0.0022	0.5186	0.0166	0.0601	0.0006	688.59	74.07	424.24	11.12	376.22	3.45
D3-22	0.85	71.82	657.08	793.46	0.0504	0.003	0.1437	0.0077	0.0209	0.0004	213.04	134.24	136.38	6.85	133.31	2.51
D3-23	0.48	9.43	73.41	152.82	0.0489	0.0035	0.1423	0.0094	0.021	0.0003	142.68	162.94	135.05	8.39	134.04	2.08
D3-24	0.41	63.75	143.97	353.19	0.0588	0.0017	0.5962	0.0171	0.0734	0.0007	566.70	60.18	474.81	10.89	456.58	4.46
D3-25	1.24	56.88	209.01	165.83	0.0563	0.0026	0.4051	0.0174	0.0529	0.0007	464.86	99.07	345.34	12.57	332.09	3.99
D3-26	1.43	88.34	914.13	636.22	0.0486	0.0022	0.1383	0.0061	0.0207	0.0002	127.87	109.24	131.52	5.41	132.34	1.44
D3-27	0.89	101.26	534.54	601.79	0.0511	0.0015	0.2627	0.0075	0.0371	0.0003	255.62	73.14	236.85	6.05	234.98	1.93
DZ5																
DZ5-1	0.60	10.89	92.41	150.49	0.0545	0.0013	0.3064	0.0084	0.0408	0.0011	392.00	50.39	271.40	6.50	257.70	6.51
DZ5-2	0.56	58.84	356.68	424.94	0.0663	0.0021	1.2407	0.0411	0.1358	0.0038	814.20	64.23	819.20	18.61	821.10	21.64

(Continued on following page)

TABLE 2 | (*Continued*) LA–ICP–MS U–Pb isotopic data for zircons from the lamprophyres in the Tuquan Basin.

Spot	Th/U	Contents ($\times10^{-6}$)			$^{207}Pb/^{206}Pb$		$^{207}Pb/^{235}U$		$^{206}Pb/^{238}U$		$^{207}Pb/^{206}Pb$		$^{207}Pb/^{235}U$		$^{206}Pb/^{238}U$	
		Pb	Th	U	Ratio	1σ	Ratio	1σ	Ratio	1σ	Age (Ma)	1σ	Age (Ma)	1σ	Age (Ma)	1σ
DZ5-3	0.60	10.89	92.41	150.49	0.0513	0.0017	0.1333	0.0047	0.0188	0.0005	255.10	74.48	127.10	4.18	120.30	3.31
DZ5-4	0.82	26.21	125.94	156.67	0.0559	0.0013	0.3124	0.0086	0.0405	0.0011	449.40	50.18	276.00	6.63	255.90	6.53
DZ5-5	0.63	30.40	145.84	230.39	0.054	0.0018	0.2855	0.0098	0.0384	0.0011	369.00	71.41	255.00	7.75	242.70	6.67
DZ5-6	0.83	16.31	108.60	129.38	0.0521	0.0017	0.1935	0.0066	0.0269	0.0008	290.60	71.90	179.60	5.63	171.20	4.72
DZ5-7	0.44	34.78	101.06	166.29	0.0515	0.0013	0.2307	0.0067	0.0325	0.0009	264.60	57.11	210.80	5.55	206.00	5.41
DZ5-8	0.52	16.43	143.41	279.15	0.051	0.0017	0.1466	0.0051	0.0208	0.0006	240.50	74.99	138.90	4.55	133.00	3.73
DZ5-9	0.41	9.36	73.33	176.07	0.053	0.0015	0.2593	0.0082	0.0355	0.001	328.30	64.22	234.10	6.62	224.80	6.08
DZ5–10	0.27	30.92	42.28	158.59	0.0561	0.0014	0.3749	0.0109	0.0484	0.0013	456.60	55.16	323.30	8.05	304.90	8.00
DZ5-11	0.56	34.04	287.91	514.18	0.0583	0.0014	0.3783	0.0107	0.047	0.0013	542.60	51.58	325.80	7.86	296.20	7.72
DZ5-12	0.28	29.39	154.73	544.91	0.0517	0.0017	0.1628	0.0058	0.0228	0.0007	273.10	75.33	153.10	5.03	145.50	4.10
DZ5-13	0.64	22.49	202.78	316.11	0.0521	0.0016	0.1986	0.0066	0.0277	0.0008	287.60	69.51	184.00	5.63	176.00	4.87
DZ5-14	0.45	12.68	102.84	225.08	0.0555	0.0016	0.3694	0.0116	0.0483	0.0013	430.00	62.15	319.20	8.62	304.20	8.23
DZ5-15	0.45	35.01	103.41	260.37	0.0506	0.0016	0.1748	0.0059	0.025	0.0007	224.20	71.77	163.60	5.12	159.40	4.45
DZ5-16	1.13	109.12	359.28	317.72	0.0495	0.0014	0.1626	0.0052	0.0238	0.0007	170.20	65.97	153.00	4.52	151.90	4.16
DZ5-17	0.85	71.82	657.08	793.46	0.0573	0.0015	0.6534	0.0191	0.0828	0.0023	501.10	55.38	510.60	11.72	512.50	13.41
DZ5-18	0.60	15.59	114.24	192.90	0.0491	0.0018	0.1323	0.005	0.0196	0.0006	151.50	82.58	126.20	4.47	124.90	3.59
DZ5-19	0.48	9.43	73.41	152.82	0.0487	0.0021	0.1314	0.0057	0.0196	0.0006	133.70	97.92	125.40	5.09	124.90	3.79
DZ5-20	0.41	63.75	143.97	353.19	0.051	0.0012	0.2802	0.008	0.0399	0.0011	238.30	55.26	250.80	6.37	252.20	6.67
DZ5-21	1.43	88.34	914.13	636.22	0.0524	0.0016	0.2372	0.0079	0.0328	0.0009	304.10	68.50	216.20	6.47	208.20	5.82
DZ5-22	0.62	65.73	128.75	205.98	0.1115	0.0029	4.9949	0.1446	0.325	0.0092	1823.70	45.71	1818.50	24.49	1814.30	44.72
DZ5-23	0.89	101.26	534.54	601.79	0.044	0.0024	0.1194	0.0063	0.0197	0.0007	0.10	17.80	114.50	5.74	125.60	4.12
DZ5-24	0.65	57.30	541.00	835.28	0.0526	0.0022	0.1649	0.0070	0.0227	0.0006	312.8	91.84	155	6.06	144.9	3.61
DZ5-25	0.73	25.46	232.75	335.33	0.0587	0.0019	0.1665	0.0056	0.0206	0.0005	555.7	68.41	156.4	4.85	131.3	3.17
DZ5-26	0.38	65.39	273.01	601.07	0.0571	0.0021	0.1580	0.0058	0.0201	0.0006	492.8	77.92	148.9	5.1	128.2	3.7
DZ5-27	0.80	45.72	226.71	282.10	0.0551	0.0022	0.1719	0.0070	0.0226	0.0007	415.1	87.56	161.1	6.06	144.3	4.26
DZ5-28	0.65	57.30	541.00	835.28	0.0587	0.0021	0.1543	0.0056	0.0191	0.0006	555.8	75.26	145.7	4.93	121.8	3.46

A total of 28 zircons were tested for sample DZ5. The results revealed relatively concordant $^{206}Pb/^{238}U$ and $^{207}Pb/^{235}U$ ratios, suggesting that the U–Pb system in the zircons had remained in a closed state and had not lost Pb after formation. The analysis of eight test points yielded a weighted mean age of 126.2 ± 2.5 Ma (MSWD = 1.6), representing the age of crystallization of the lamprophyre (**Figure 3C**; **Table 2**). The other 20, relatively old, zircons were likely to have been inherited zircons within the sample.

4.2 Major and Trace Element Contents

The results of the major and trace element analyses are listed in **Table 3**. The major element contents were normalized to 100% on an LOI-free basis before plotting them in diagrams. The petrography of these samples (as described above), combined with these geochemical data, enabled the division of the lamprophyre intrusions into two types. The Late Jurassic lamprophyre was found to consist primarily of biotite and orthoclase, and was thus referred to as the biotite orthoclase lamprophyre (BOL), while the Early Cretaceous lamprophyre was determined to predominantly comprise quartz and magnetite as accessory minerals, in addition to biotite and orthoclase, and was thus called the quartz magnetite lamprophyre (QML). For the BOL, three samples were collected from the dike with thicknesses of approximately 4–6 m (**Figure 2A**). All three samples were distributed northeast in terms of orientation, and had the same petrographic characteristics (**Table 1**). We selected M1 to represent the BOL for the major and trace element analyses.

4.2.1 Late Jurassic Lamprophyre (BOL)

The BOL (sample M1) had 56.06 wt.% of SiO_2 and a high content of total alkalis (Na_2O + K_2O) of 7.89 wt.%. It was classified as trachyandesite (Middlemost, 1994) (**Figure 4A**). In addition, its K_2O content was 5.54 wt.%, and it had a high K_2O/Na_2O ratio of 2.36. Because of this, it was plotted in the shoshonitic series (**Figure 4B**). The BOL had low contents of P_2O_5 (0.69 wt.%), CaO (1.78 wt.%), and F_2O_3 (1.72 wt.%), and high contents of MgO (4.81 wt.%), Na_2O (2.35 wt.%), FeO (4.43 wt.%), FeO^T (5.98 wt.%), Al_2O_3 (16.25 wt.%), and TiO_2 (1.51 wt.%). It had a Ti/Y ratio of 488 and an Mg# value of 58.92.

In the chondrite-normalized rare Earth element (REE) pattern (**Figure 5A**), the BOL was rich in light rare Earth elements (LREEs) [$(La/Yb)_N$ = 11.1] relative to heavy rare Earth elements (HREEs). No Eu anomaly was noted (Eu/Eu* = 1.00), and the ∑REE content was 173 ppm. In the primitive mantle-normalized spider diagram (**Figure 5B**), the BOL was rich in large-ion lithophile elements (LILEs; e.g., Ba, K, and Pb) and depleted in elements with a high field strength (HFSEs; e.g., Nb, Ta, and Ti).

4.2.2 Early Cretaceous Lamprophyres (QMLs)

The QML samples (D3, DZ5, and DZ12) had SiO_2 contents of 57.13–62.57 wt.% and high total alkali (Na_2O + K_2O) contents of 7.10–8.48 wt.%. They were classified as ranging from trachyandesite to trachyte (**Figure 4A**). They had K_2O contents of 1.93–4.88 wt.% and low K_2O/Na_2O ratios ranging from 0.37 to 1.60, which led to them being plotted in the shoshonitic to the high-K calc-alkaline and

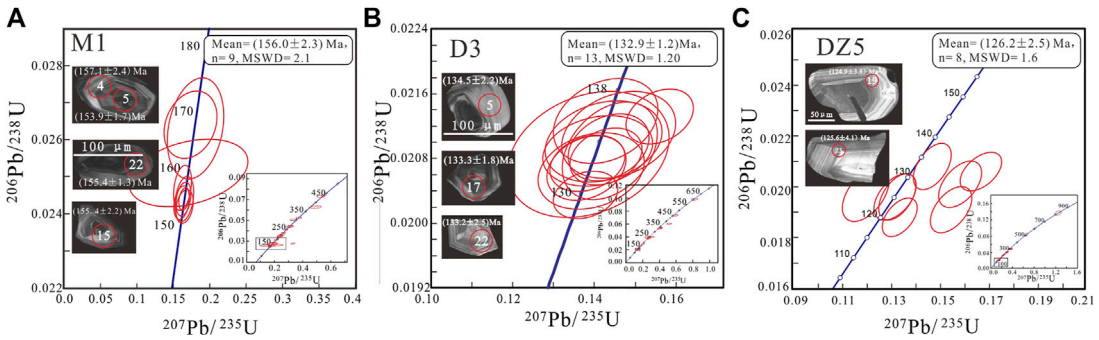

FIGURE 3 | LA–ICP–MS zircon U–Pb concordia diagrams for lamprophyres **(A)** M1, **(B)** D3, and **(C)** DZ5 in the Tuquan Basin. The insets show typical CL images of zircons with U–Pb ages.

calc-alkaline series (**Figure 4B**). The QMLs had low contents of P_2O_5 (0.56–1.09 wt.%), CaO (0.49–2.38 wt.%), and FeO (0.92–1.15 wt.%), and high contents of MgO (1.50–4.23 wt.%), Na_2O (3.05–5.17 wt.%), F_2O_3 (6.41–7.20 wt.%), FeO^T (6.92–7.40 wt.%), TiO_2 (1.34–1.53 wt.%), and Al_2O_3 (13.21–13.99 wt.%). They had a Ti/Y ratio of 203–349 and Mg# values of 27–52.

In the chondrite-normalized REE pattern (**Figure 5A**), the QML samples were rich in LREEs [$(La/Yb)_N$ = 34.4–39.0] relative to HREEs, featured Eu anomalies (Eu/Eu* = 0.88–0.93), and their ∑REE contents ranged from 361 to 694 ppm. In the primitive mantle-normalized spider diagram (**Figure 5B**), the QMLs were rich in LILEs (e.g., Ba, K, and Pb) and strongly depleted in HFSEs (e.g., Nb, Ta, and Ti).

5 DISCUSSION

5.1 Timing of Formation of the Lamprophyres

Zircons from the Late Jurassic lamprophyre (BOL) and Early Cretaceous lamprophyres (QMLs) exhibited striped absorption that was visible in the CL images, and is characteristic of zircons derived from mafic magmas. This magmatic origin is also supported by their relatively high Th/U ratios (0.2–1.43; Hoskin and Schaltegger, 2003). The U-Pb dating of these zircons should therefore yield the time of formation of the lamprophyres. The BOL (sample M1) yielded the youngest age of 156.0 ± 2.3 Ma, representing their time of formation. The QMLs (D3 and DZ5) yielded the youngest $^{206}Pb/^{238}U$ ages of 132.9 ± 1.2 and 126.2 ± 2.5 Ma, respectively, indicating the timing of formation of the lamprophyres. The Late Jurassic–Early Cretaceous ages were similar to those of the U-Pb dating (164–130 Ma) of high-K volcanic rocks in the Erguna–Xing'an–Songliao Blocks (Tang et al., 2015; Ji et al., 2021). They are also consistent with the results of U–Pb dating of Mesozoic intrusions and basalts in northeast China (Wang et al., 2006; Zhang et al., 2010; Wu et al., 2011; Zhang et al., 2011; Xu et al., 2013). The time of formation of the lamprophyres in the western Songliao Basin is therefore consistent with a widespread Late Jurassic–Early Cretaceous magmatic event that occurred in northeast China (**Figure 6**).

5.2 Petrogenesis

5.2.1 Alteration Effects

Before any inference can be made regarding the characteristics of the parental magma source of the lamprophyres, it is necessary to assess the possible effects of alteration on the whole-rock geochemical composition. The lamprophyre samples were characterized by variably high LOI values (2.58–4.60 wt.%), which indicates that they might have undergone low-grade metamorphism or variable degrees of alteration.

Because Zr and Th are considered to be the most immobile elements during low-grade alteration and metamorphism, they are preferred as an alteration-independent index of geochemical variation in igneous rocks. We used this to evaluate the mobility of other elements during alteration. The contents of HFSEs (such as Nb and Ta), LILEs (e.g., K and Rb), LREEs (e.g., La, Ce, and Nd), HREEs (such as Yb), and U were strongly correlated with Zr and Th (**Figure 7**) in the lamprophyre samples, which indicates that these elements were also essentially immobile during post-magmatic processes. The lamprophyre samples were characterized by subparallel patterns of elemental concentrations on chondrite- and primitive mantle-normalized trace element diagrams (**Figure 5**), which demonstrates the relative immobility of most elements at a whole-rock scale. Moreover, fresh lamprophyres may also have high LOI values (Rock, 1991). We conclude that post-magmatic processes had only minor effects on the chemical compositions of the studied samples, and high LOI values were intrinsic to the lamprophyres.

5.2.2 Effect of Continental Crustal Contamination

Before trying to assess the characteristics of the mantle source of these mafic dikes, it is important to consider the effects of crustal contamination that is also common in the generation of mantle-derived rocks. Evidence suggests that crustal contamination did not play a significant role in the petrogenesis of the lamprophyres. Such evidence includes the following: 1) The lamprophyres occurred as dike swarms, suggesting a rapid ascent through the crust. 2) The minerals in the lamprophyres were euhedral crystals, such as biotite and orthoclase. 3) The lamprophyres had incompatible elemental concentrations—for instance those of Sr (173–1506 ppm), Ba (616–1787 ppm), K_2O (1.93–5.54 wt.%), and Nd (30.2–137.4 ppm)—that were higher than those of the bulk

TABLE 3 | Major (wt.%) and trace element (ppm) compositions of the lamprophyres.

Lithology	BOL	QMLs		
Sample	M1	D3	DZ5	DZ12
Major element (wt.%)				
SiO_2	56.06	57.13	62.08	62.57
TiO_2	1.51	1.34	1.53	1.52
Al_2O_3	16.25	13.99	13.21	13.98
Fe_2O_3	1.72	6.41	7.20	6.63
FeO	4.43	1.15	0.92	1.08
FeO^T	5.98	6.92	7.40	7.05
MnO	0.06	0.11	0.10	0.14
MgO	4.81	4.23	2.16	1.50
CaO	1.78	2.38	1.17	0.49
Na_2O	2.35	3.05	5.17	4.91
K_2O	5.54	4.88	1.93	3.57
P_2O_5	0.69	1.09	0.95	0.56
LOI	4.60	3.90	3.17	2.58
Total	99.81	99.66	99.60	99.53
Mg#	58.92	52.13	34.23	27.51
$K_2O + Na_2O$	7.89	7.93	7.10	8.48
K_2O/Na_2O	2.36	1.60	0.37	0.73
Trace element (ppm)				
La	26.4	127.1	97.7	76.9
Ce	65.9	280.3	211.3	132.3
Pr	7.6	34.7	25.5	18.9
Nd	30.2	137.4	98.3	70.5
Sm	6.14	25.47	18.68	12.90
Eu	1.96	7.20	5.02	3.46
Gd	5.64	20.55	15.11	9.84
Tb	0.79	2.27	1.77	1.18
Dy	4.00	9.57	7.97	5.40
Ho	0.76	1.50	1.26	0.89
Er	1.98	3.45	2.97	2.08
Tm	0.28	0.44	0.35	0.25
Yb	1.70	2.34	2.03	1.55
Lu	0.27	0.36	0.29	0.22
Rb	73.4	101.3	14.5	28.3
Ba	991	1787	616	1167
Th	7.55	21.03	20.64	15.71
U	2.39	4.86	5.45	4.57
Nb	19.6	19.8	22.9	23.2
Ta	1.36	1.54	0.83	0.83
K	45.765	40.313	15.943	29.491
Pb	11.64	28.91	39.68	31.07
Sr	173	1506	501	599
P	3012	4757	4146	2444
Zr	455	503	580	593
Hf	14.18	14.07	15.11	15.30
Sc	10.88	15.27	14.29	12.62
V	160.0	162.7	170.6	163.8
Cr	166.5	126.1	31.2	23.8
Co	22.5	23.9	17.7	15.5
Ni	94.1	54.8	23.7	19.8
Ga	20.0	22.0	19.5	17.5
Y	19.6	41.9	38.2	25.4
Cs	1.00	3.59	2.20	3.41
δEu	1.00	0.93	0.88	0.90
$(La/Yb)_N$	11.15	39.01	34.48	35.59
∑REE	173.15	694.54	526.35	361.73
Rb/Sr	0.42	0.06	0.02	0.04

(Continued in next column)

TABLE 3 | (*Continued*) Major (wt.%) and trace element (ppm) compositions of the lamprophyres.

Lithology	BOL	QMLs		
Sample	M1	D3	DZ5	DZ12
Ba/Rb	13.5	17.6	42.6	41.2
Dy/Yb	2.35	4.09	3.92	3.48
K/Yb*1000	28.3	17.9	8.13	19.63

Note: $FeO^T = FeO+0.8998*Fe_2O_3$. LOI, loss on ignition. Mg# = 100× molar Mg/(Mg + Fe^T). $\delta Eu = Eu_N/(Sm_N \times Gd_N)^{0.5}$. REE, rare earth elements.

continental crust (average abundances of Sr, Ba, K_2O, and Nd in the crust were 320 ppm, 456 ppm, 1.81 wt.%, and 20 ppm, respectively; Rudnick and Gao, 2003). 4) The lamprophyres had Nb/Ta (12.8–27.4) and Zr/Hf (32.1–38.7) ratios similar to those of the primitive mantle (17.5 ± 0.2 and 36.27 ± 2.0, Taylor and McLennan, 1985), and much higher than those of the continental crust (11 and 33, Taylor and McLennan, 1985). 5) The Lu/Yb ratios are considered to be an indicator of crustal contamination. The continental crust was characterized by high Lu/Yb (0.16–0.18) ratios while mantle-derived magmas had low Lu/Yb (0.14–0.15) ratios (Sun and McDonough, 1989). The low Lu/Yb (0.14–0.15) ratios of the lamprophyres were similar to those of the mantle-derived magmas, thus ruling out the prospect of noticeable crustal contamination. 6) Fifty-four concordant analyses of the rocks of the walls, e.g., the Jurassic sedimentary rocks. yielded two age populations at 160.0–185.4 Ma (n = 47) and 222.1–274 Ma (n = 7) (unpublished LA–ICP–MS U-Pb data). Eighty concordant analyses of the lamprophyres yielded six age populations at 120.3–144.9 Ma (n = 23), 145.5–160.1 Ma (n = 10), 162.0–185.5 Ma (n = 9), 191.3–296.2 Ma (n = 23), 303.1–376.2 Ma (n = 8), and 432–1832.7 Ma (n = 7). The youngest analyses yielded ages of the lamprophyres lower than those of the Jurassic sedimentary rocks. In addition, nine analyses of the lamprophyres yielded ages of 162.0–185.5 Ma, much lower than those of the Jurassic sedimentary rocks, which yielded ages of 160.0–185.4 Ma over 47 analyses. These results suggests that the youngest ages of the lamprophyres can represent their age of formation, and crustal contamination did not play a major role in this process.

5.2.3 Magma Sources and the Nature of the Lamprophyre

Mafic rocks are generally considered to be mantle-derived melts. In particular, lamprophyres are considered to be the products of the partial, low-degree melting of the enriched subcontinental lithosphere mantle (Rock, 1987; Gibson et al., 2006; Choi et al., 2020). The lamprophyres in the Tuquan Basin are characterized by high contents of FeO^T, MgO, and TiO_2, high Mg# values, strong fractionation between LREEs and heavy (H) REEs, LILE enrichment, and HFSE depletion. These geochemical signatures are similar to those of contemporaneous arc-like mafic rocks for which the magmas were interpreted to have originated from the lithospheric mantle source (Tang et al., 2015; Zhang et al., 2020; Ji et al., 2021). Moreover, the Lu/Yb ratios of the BOL and QML

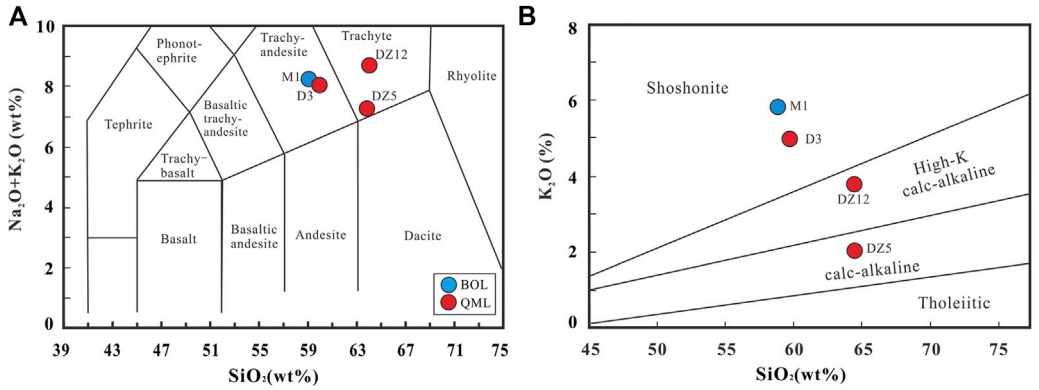

FIGURE 4 | (A) SiO_2 vs. ($Na_2O + K_2O$) classification diagram (modified after Middlemost, 1994). **(B)** SiO_2 vs. K_2O Diagram (after Peccerillo and Taylor, 1976) of the lamprophyres in the Tuquan Basin.

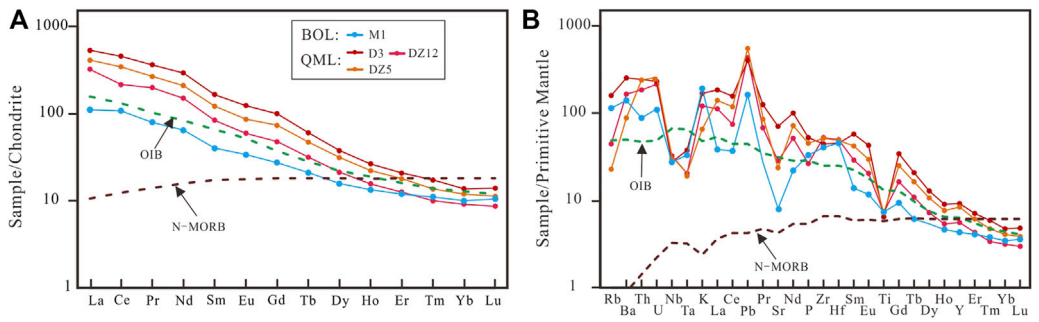

FIGURE 5 | (A) chondrite-normalized REE pattern and **(B)** primitive mantle-normalized spider-diagram of the lamprophyres in the Tuquan Basin. Data sources: chondrite (Sun and McDonough, 1989), primitive mantle (Sun and McDonough, 1989), N-MORB, and OIB (Sun and McDonough, 1989).

samples, ranging from 0.14 to 0.15, were similar to the range for mantle magmas (0.14–0.15, Sun and McDonough, 1989) rather than the continental crust (0.16–0.18, Sun and McDonough, 1989). The BOL and QML samples exhibited low ratios of Zr/Ba (0.28–0.94), and high ratios of La/Ta and La/Nb (9.33–117.26 and 1.34–6.43, respectively), close to the ratios of the region of the lithospheric magma source (Thompson and Morrison, 1988; Menzies et al., 1991). The BOL and QML samples had high Sr contents (173–1506 ppm) and lacked significant Eu anomalies ($Eu/Eu^* = 0.88–1.00$), indicating that they had originated from a mantle source (Rapp and Watson, 1995). In addition, the high LREE/HREE ratios of the lamprophyre samples are often assumed to be caused by the partial melting of a metasomatized lithospheric mantle (Guo et al., 2004). Furthermore, the trace element compositions of the lamprophyres were neither Mid-Ocean Ridge Basalt (MORB) like nor Ocean Island Basalt (OIB) like, indicating that the lamprophyres had not derived from MORB- or OIB-type sources within the asthenospheric mantle (Sun and McDonough, 1989).

In terms of the pattern of distribution of the trace elements, the BOL and QML samples were rich in LREEs and LILEs and depleted in HREEs and HFSEs (Nb, Ta, and Ti), suggesting that the magmas had derived from an enriched lithospheric mantle that had previously been modified by interaction with subducted slab material (Tarney and Jones, 1994). The BOL and QML samples exhibited relatively high ratios of Ba/Nb, Ba/Ta, and Ba/Th (26.93–90.43, 726.46–1398.27, and 29.84–84.97, respectively), and a low ratio of La/Sm (4.99–5.95), suggesting that a subduction-modified continental lithospheric mantle had been involved in the magma source for the lamprophyres (Fitton et al., 1988; Genç and Tüysüz, 2010).

The characteristics of the trace element of the samples in **Figure 8** show that the sources of the lithospheric mantle of the BOL and QMLs were formed at an active continental margin, and had been previously metasomatized by subduction-related fluids. The Ba/Nb vs. La/Nb diagram in **Figure 8A** indicates that the lamprophyres showed lithologic affiliation to the volcanic arc. The Th/Yb vs. Ta/Yb diagram in **Figure 8B** shows the characteristics of the lamprophyres formed at an active continental margin. The Th/Y vs. Sm/Th diagram in **Figure 8C** shows that the BOL and QML lamprophyres originated from an enriched lithospheric mantle. Slab-

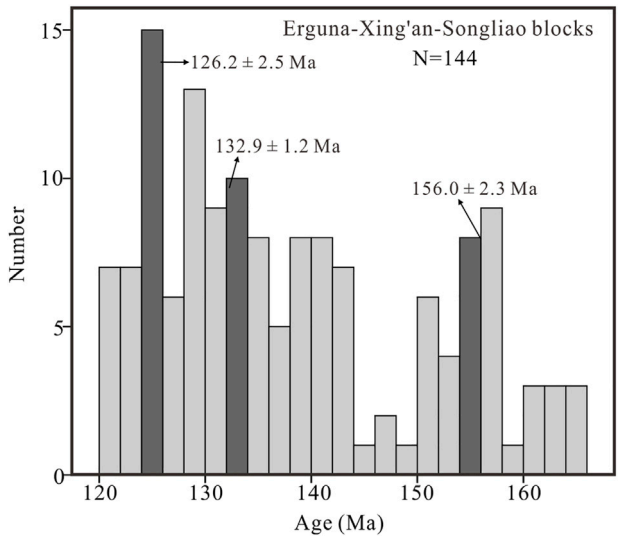

FIGURE 6 | Histogram of the U–Pb ages of zircons from Mesozoic igneous rocks in the Erguna-Xing'an-Songliao Blocks. Age data sources: Wang et al., 2006; Zhang et al., 2010; Wu et al., 2011; Tang et al., 2015; Li et al., 2018; Ji et al., 2020, 2021 and this study.

released fluids or melts would have metasomatized the overlying lithospheric mantle and led to them being rich in LILE elements, such as K, Sr, and Pb. As shown in **Figure 8D**, the BOL and QML samples exhibited Nb/U ratios of 8.2 and 4.0–5.0, respectively. These values are significantly lower than those of the MORB (47 ± 10, Hofmann et al., 1986) and the OIB (47 ± 10, Hofmann et al., 1986). They are also lower than the values of the upper crust (9, Taylor and McLennan, 1985) and the lower crust (21, Taylor and McLennan, 1985). However, the Nb/U values of the lamprophyres were similar to those of the subduction zone-related hydrous fluids and the global average for subducted sediments (Nb/U = 5, Plank and Langmuir, 1998). These results suggest that the lamprophyres recorded the fluid-related metasomatism of the region of their lithospheric mantle source as a result of subduction (Hofmann, 1997). The Ba/Th vs. La/Sm diagram in **Figure 8E** shows that the mantle source was primarily influenced by slab dehydration (Genç and Tüysüz, 2010). Some HFSEs signatures can be used to distinguish between the roles of fluids and melts as metasomatizing agents (Polat and Hofmann, 2003). The BOL and QMLs had low ratios of Th/Zr (0.01–0.04) and Nb/Zr (0.03–0.04) (**Figure 8F**), indicating that the magma source had been affected by the metasomatism of the fluid.

5.2.4 Source Mineralogy and Depth

The Late Jurassic BOL and Early Cretaceous QML samples had high K_2O contents and were rich in LILEs. The volatility-enriched minerals, such as amphiboles and phlogopites, were the primary host minerals for K and LILEs in the lithospheric mantle (Foley et al., 1996; Ionov et al., 1997). Melts in equilibrium with amphibole in the source were expected to have a significantly low Rb/Sr ratio (0.1) and a high Ba/Rb ratio (>20), whereas melts from a phlogopite-containing source region had a relatively high Rb/Sr ratio (>0.1) and a low Ba/Rb ratio (<20) (Furman and Graham, 1999; Ma et al., 2014). The BOL exhibited a high Rb/Sr ratio of 0.42 (>0.1) and a low Ba/Rb ratio of 13.5 (<20), indicating that it had involved a magma source of phlogopite-containing, enriched lithospheric mantle (**Figure 9**). The QML samples had a low Rb/Sr ratio of 0.02–0.06 (<0.1) and a high Ba/Rb ratio of 17.6–42.6 (on average, 33.8), indicating a magma source from an amphibole-containing and enriched lithospheric mantle (**Figure 9**).

The K/Yb vs. Dy/Yb diagram can be used to constrain regions of the magma source and the degree of partial melting, and to distinguish between partial melting in the spinel and the garnet stability fields of a phlogopite- and/or amphibole-bearing lherzolite (Duggen et al., 2005). Melts formed from partial melting had relatively high and low Dy/Yb ratios (>2.5 and <1.5, respectively) in the stable areas for garnet and spinel, respectively (Duggen et al., 2005). The K/Yb ratio corresponds to the degree of partial melting. The BOL sample had a Dy/Yb ratio of 2.35 and a K/Yb*1000 ratio of 28.3. The projected point of the BOL sample fell between the curves of partial melting of garnet-facies phlogopite lherzolite and spinel-facies lherzolite, corresponding to a degree of melting of 10% (**Figure 10A**) and implying that the partial melting had likely occurred in the spinel–garnet transition zone. In the REE melting model for mantle peridotites (**Figure 10B**), the projected point of the BOL sample was found to fall on the curve of a mixture of garnet peridotite and spinel peridotite at a ratio of 7:3. The QML samples exhibited Dy/Yb ratios of 3.48–4.09 and K/Yb*1000 ratios of 8.13–19.63. Their projected points fell between curves of partial melting of garnet-facies lherzolite and garnet-facies amphibole lherzolite, corresponding to degrees of melting of 1%–3.5% (**Figure 10A**). In the REE melting model for mantle peridotites (**Figure 10B**), the projected points of the QML samples were found to fall on the curves for garnet peridotite and spinel peridotite mixed at different ratios (proportion of garnet >90%).

What is the mechanism driving the melting of the mantle at different depths? The upwelling of the asthenosphere triggers the decompression-induced melting of the mantle (McKenzie and Bickle, 1988). Conditions for the contemporaneous partial melting of the mantle at different depths can be satisfied if the top of the asthenosphere window reaches a certain depth (Luo et al., 2006). The thickness of the lithosphere controls this depth, and thus limits the extent of decompression-induced melting and equilibrium pressure/depth of the melt extraction, i.e., the lid effect (Ellam, 1992; Niu, 2021). Experiments have shown that the minimum pressure at which garnet is stable on the anhydrous solidus of fertile peridotite is 2.8 GPa, corresponding to a depth of about 85 km (Robinson and Wood, 1998). The maximum depth of the spinel–garnet transition zone is 60–70 km (McKenzie and O'Nions, 1991; Klemme and O'Neill, 2000). The above analyses were used to plot the melting curves of the BOL and the QML samples for lherzolite (**Figure 10B**). They have relatively low and high garnet/spinel ratios (<2.3 and >9, respectively). We suggest that the BOL (156.0 ± 2.3 Ma) was likely derived from the high-degree partial melting of the phlogopite-bearing lherzolite mantle

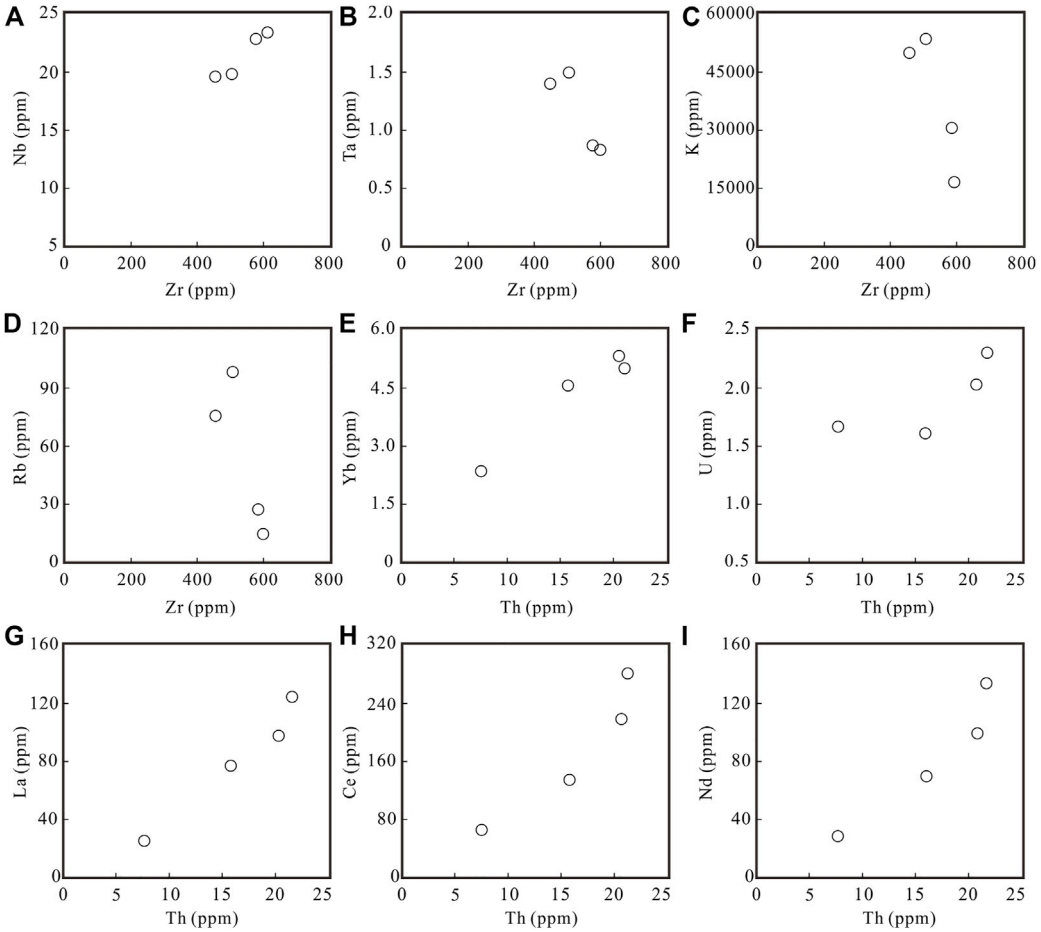

FIGURE 7 | Diagrams showing variations of selected elements **(A)** Nb, **(B)** Ta, **(C)** K, **(D)** Rb vs. Zr and **(E)** Yb, **(F)** U, **(G)** La, **(H)** Ce, **(I)** Nd vs. Th in the lamprophyre samples to check for element mobility during post-magmatic alteration.

in the spinel–garnet transition zone at a depth of about 60 km. The older QML (132.9 ± 1.2 Ma) was likely derived from the low-degree partial melting of the lherzolite mantle in the garnet zone at a depth of ca. 85 km. The younger QML (126.2 ± 2.5 Ma) had lower Dy/Yb ratios (3.48–3.92) than the older QML (132.9 ± 1.2 Ma), with a Dy/Yb ratio of 4.09 implying that the younger magma had been produced at a shallower depth of the mantle (<85 km) than the older one. Thus, from 156 Ma to 132 Ma, the lithosphere in the study area thickened by approximately 25 km at a rate of approximately 1.0 km/Myr.

5.3 Geodynamics

5.3.1 Changes in the Thickness of the Lithosphere

The Manzhouli–Suifenhe geoscience transect in northeast China, which is part of the Global Geoscience Transect (GGT) Project, extends from Manzhouli in the west to Suifenhe in the east over a distance of 1300 km, and passes through the Great Xing'an Range and the Songliao Basin (see **Figure 1**).

Data on deep seismic reflections, and gravitational and magnetic data of the GGT (Yang et al., 1996) shows that the crust and lithosphere in NE China are 30–40 and 55–110 km thick at present, respectively. The thickness of the lithosphere in the Songliao Basin ranges from 55 km (in Daqing and Anda at the center of the basin) to 110 km (at the eastern margin of the basin in Shangzhi). The lithosphere in the Great Xing'an Range is 76–90 km thick, and is 80 km thick in the Tuquan Basin (**Figure 11**).

The depths at which the magmas of the BOL and QMLs originated in the Tuquan Basin, as calculated in this study, show that the lithospheric thickness in NE China thickened from 156.0 ± 2.3 Ma to 132.9 ± 1.2 Ma and then thinned from 132.9 ± 1.2 Ma to 126.2 ± 2.5 Ma (**Figure 12**). The thickness of the lithosphere in this period fluctuated within a range of magnitude that it has at present.

5.3.2 Cause of the Thickening of the Lithosphere

During the Late Mesozoic, the tectonics of the study area were involved in both the subduction of the Paleo-Pacific plate beneath the Eurasian continental margin (Guo et al., 2015; Wang et al., 2019) and tectonic events related to the Mongol–Okhotsk Suture Zone (Tang et al., 2015; Liu et al., 2018).

In the Erguna and Xing'an Blocks volcanic rocks from the Early-to-Middle Jurassic (193–164 Ma) are thought to have

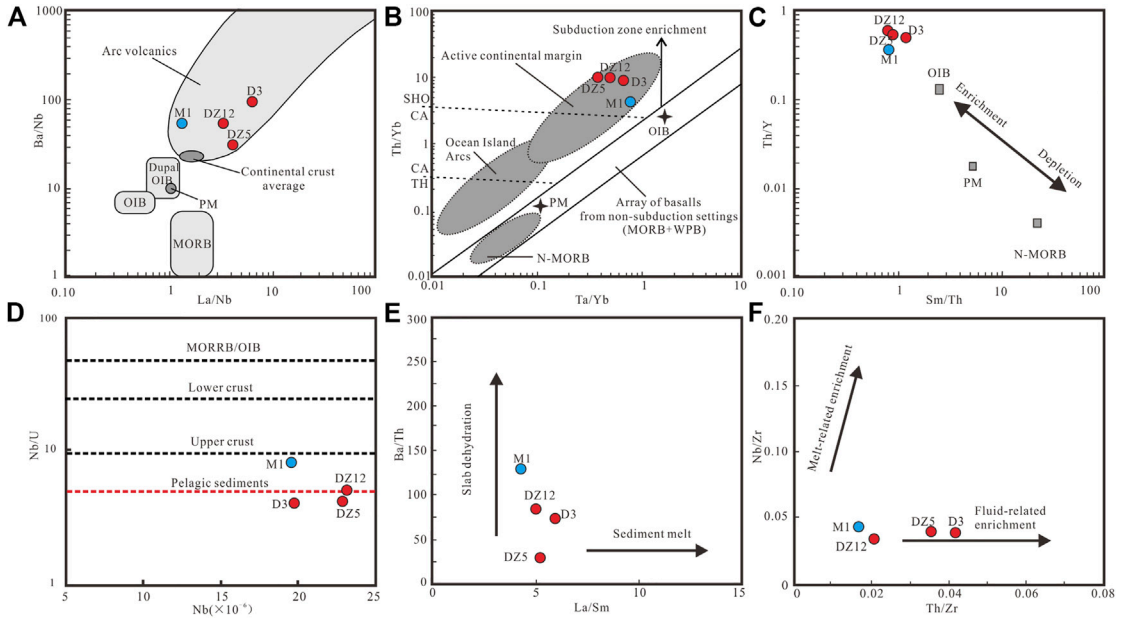

FIGURE 8 | Plot of **(A)** Ba/Nb vs. La/Nb (after Niu et al., 2017). **(B)** Th/Yb vs. Ta/Yb (after Pearce, 1983). **(C)** Th/Y vs. Sm/Th (after Su et al., 2012), the reference fields for primitive mantle (PM), OIB, and N-MORB are from Sun and McDonough (1989). **(D)** Nb/U vs. Nb diagram for the lamprophyres in the Tuquan Basin. Data sources: MORB and OIB (Hofmann et al., 1986), lower and upper crust (Taylor and McLennan, 1985), pelagic sediments (Plank and Langmuir, 1998). **(E)** Ba/Th vs. La/Sm (after Labanieh et al., 2012). **(F)** Nb/Zr vs. Th/Zr (after Kepezhinskas et al., 1997). Abbreviations are as follows: WPB, within-plate basalts; N-MORB, normal mid-ocean ridge basalts; OIB, ocean island basalts; MORB, mid-ocean ridge basalts; PM, primitive mantle; TH, tholeiitic; CA, calc-alkaline; SHO, shoshonitic.

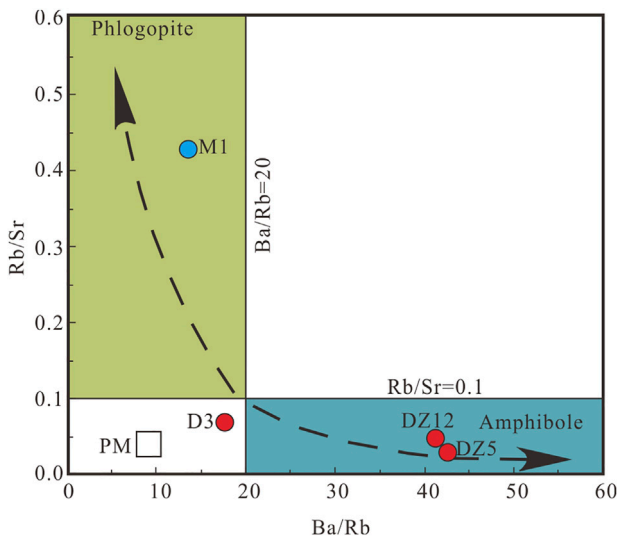

FIGURE 9 | Rb/Sr vs. Ba/Rb diagram (see e.g., Furman and Graham, 1999).

been formed in an active continental margin setting related to the southward subduction of the Mongol–Okhotsk Oceanic plate (Xu et al., 2013; Wang et al., 2015). In the Jiamusi and Songliao Blocks, volcanic rocks from the Early-to-Middle Jurassic (194–174 Ma) have been thought to have formed in an intraplate extensional setting related to the westward subduction of the Paleo-Pacific plate (Guo et al., 2015; Huang et al., 2021). There was a remarkable reduction in magmatic activity during the Late Jurassic and the Early Cretaceous (173–133 Ma) in the Jiamusi and Songliao Blocks (Xu et al., 2013; Ji et al., 2019), suggesting that subduction-related igneous activities in the Paleo-Pacific plate were waning in this period. By contrast in the Erguna and Xing'an Blocks, volcanic rocks from the Late Jurassic and the Early Cretaceous (164–124 Ma) are widely distributed (Zhang et al., 2010; Ji et al., 2021). They are related to the combined effects of the Paleo-Pacific and Mongol–Okhotsk tectonic regimes (Ouyang et al., 2015; Li et al., 2018). The question is: which of them in this region was dominant in terms of geodynamics during the Late Jurassic and the Early Cretaceous?

Based on the results of this study, we propose that the Mongol–Okhotsk tectonic regime was most likely responsible for the generation of the lamprophyres, in that space and time were coupled between the formation of lamprophyre and the tectonic event of the Mongol–Okhotsk Suture Zone. The study area is located less than 500 km from the Mongol–Okhotsk Suture (**Figure 1A**), and the closure of the Mongol–Okhotsk Ocean occurred mainly during the Jurassic and ended during the Early Cretaceous (Cogné et al., 2005; Metelkin et al., 2010). The BOL from the Late Jurassic and the QMLs from the Early Cretaceous are shoshonite and calc-alkaline in series, and were formed in an active continental margin and derived from the partial melting of an enriched lithospheric mantle that had been previously metasomatized by subduction-related fluids. In addition, these lamprophyres were coeval with the Late Jurassic and the Early Cretaceous volcanic rocks in the Erguna

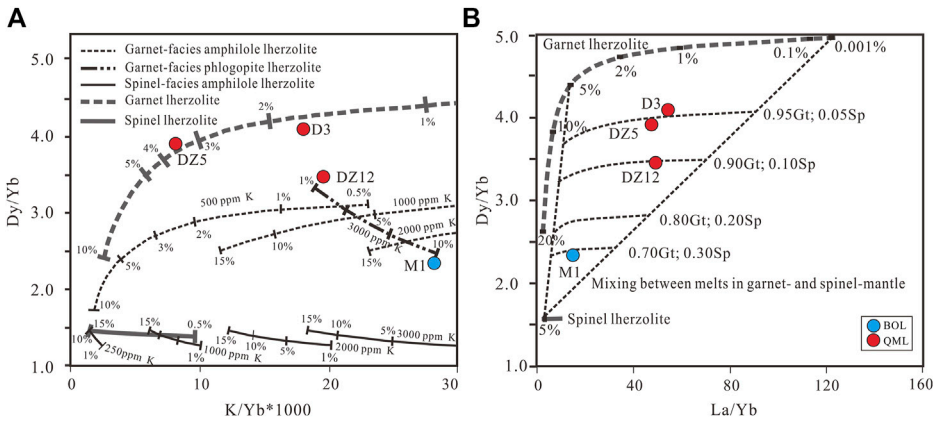

FIGURE 10 | (A) Plot of K/Yb vs. Dy/Yb for lamprophyres in the Tuquan Basin. Melting curves for garnet lherzolite, spinel lherzolite, garnet-facies phlogopite lherzolite, garnet-facies amphibole lherzolite and spinel-facies amphibole lherzolite are taken from Duggen et al. (2005). **(B)** La/Yb vs. Dy/Yb in lherzolite REE melting model is from Thirlwall et al. (1994), partition coefficients are from McKenzie and O'Nions (1991).

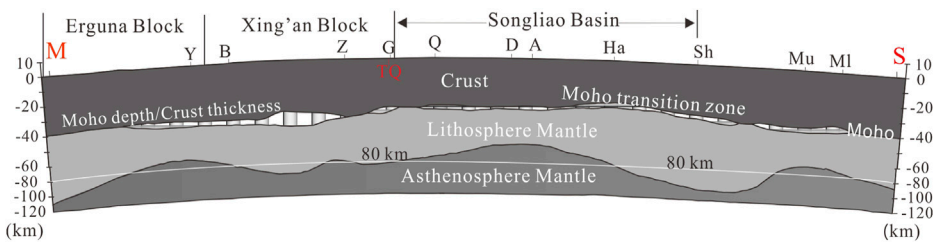

FIGURE 11 | Underlying crust and lithospheric and asthenospheric mantle of the Songliao Basin along the GGT (according to Wang et al., 2016). Cities: M, Manzhouli; Y, Yakeshi; B, Boketu; Z, Zhalantun; TQ, Tuquan; G, Gannan; Q, Qiqihaer; D, Daqing; A, Anda; Ha, Harbin; Sh, Shangzhi; Mu, Mudanjiang; Ml, Muling; S, Suifenhe.

and Xing'an Blocks, which are thought to be related to the Mongol–Okhotsk tectonic regime (Xu et al., 2013; Tang et al., 2015). The collision associated with the closure of the Mongol–Okhotsk Ocean could have caused lithospheric thickening between the Siberia and the Mongolia-China Blocks (Metelkin et al., 2010). The BOL (156.0 ± 2.3 Ma) recorded the lithospheric thickness at about 60 km and the QML (132.9 ± 1.2 Ma) recorded it at 85 km. Thus, in the period 156–132 Ma, the lithosphere in the study area thickened by approximately 25 km (**Figure 12**). It is widely believed that the delamination of a thickened lithosphere could have caused the lithosphere thinning in NE China (Wang et al., 2006; Zhang et al., 2010; Wu et al., 2011). The younger QML (126.2 ± 2.5 Ma) recorded a thinner lithosphere (< 85 km), suggesting that the lithosphere in NE China thinned from 132.9 ± 1.2 Ma to 126.2 ± 2.5 Ma.

We used the results of this study to create a three-stage model of geodynamic evolution in NE China from 156 Ma to 126 Ma, as shown in **Figure 13**. Stage A: This consisted of the southeastward subduction of the Mongol–Okhotsk oceanic crust under the counterpart continental crust, and suturing, between the Siberian craton in the northwest and the Erguna–Xing'an–Songliao Blocks in the southeast, in the Kimmeridgian and Tithonian. Stage B: This consisted of the closure of the Mongol–Okhotsk Ocean, eventually leading to continental collision between the Siberian craton and

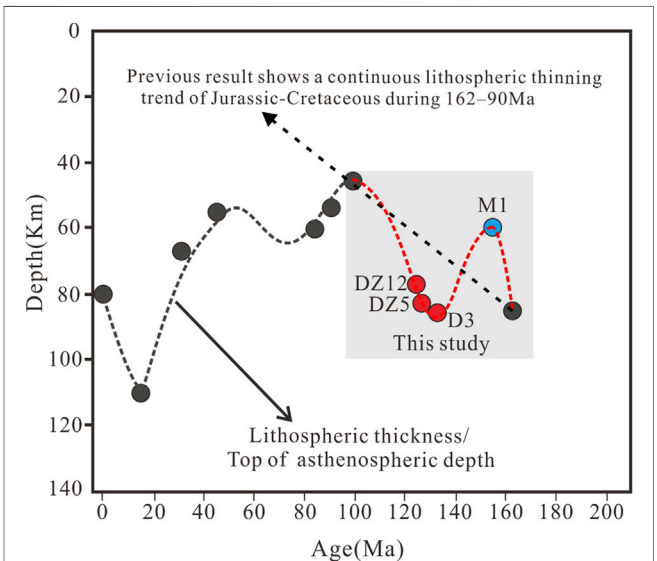

FIGURE 12 | Variation in lithospheric thickness in Northeast China (200 Ma-0 Ma). 170 Ma from Lu et al. (1996) and Huang et al. (2021); 100 Ma from Xu et al. (1994); 88 Ma from Wang et al. (2009); 92 Ma, 31 Ma, and 15 Ma from Zhang et al. (2006); 45 Ma from Zhou (2006); 0 Ma from Wang et al. (2016).

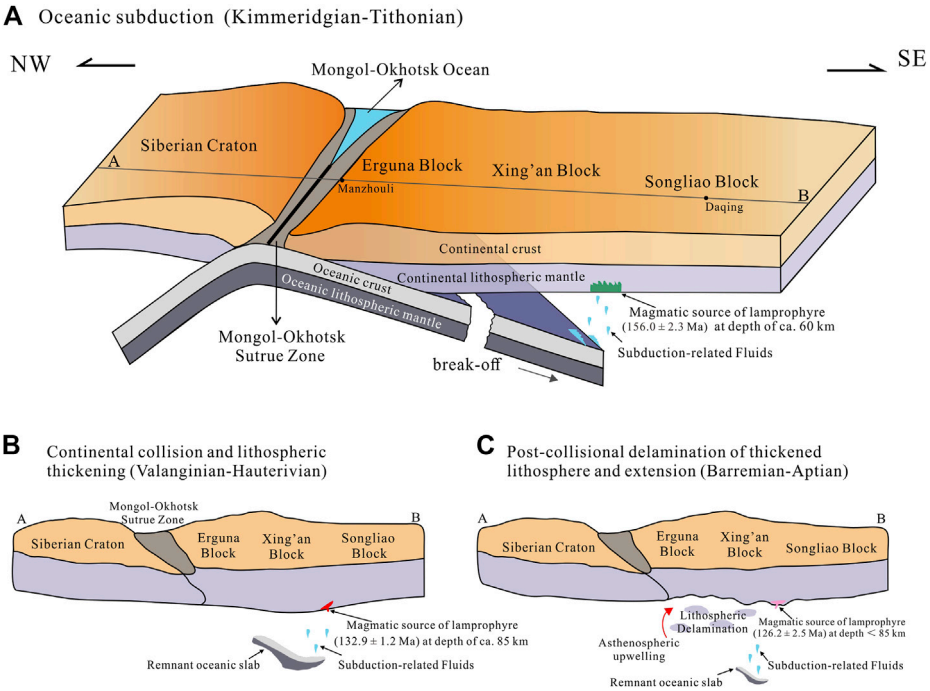

FIGURE 13 | The cartoon illustrations showing the Late Jurassic to the Early Cretaceous tectonic evolution of NE China. **(A)** the southeastward subduction of the Mongol–Okhotsk oceanic crust that resulted in the suture between the Siberian craton and the Erguna–Xing'an–Songliao Blocks in the Kimmeridgian and Tithonian; **(B)** continental collision of the related Blocks and the following lithospheric thickening near the suture zone in the Valanginian and the Hauterivian; **(C)** post-collisional delamination of the thickened lithosphere and its extension during the Barremian up to the Aptian.

Erguna–Xing'an–Songliao Blocks. The collision caused lithospheric thickening in the Valanginian and the Hauterivian. Stage C: This consisted of the post-collisional delamination of the thickened lithosphere and extension, resulting in lithospheric thinning in the Barremian and Aptian.

6 CONCLUSION

(1) The lamprophyres found along the western margin of the Songliao Basin can be categorized into two types: namely, the biotite orthoclase lamprophyre (BOL) and the quartz magnetite lamprophyre (QML). Zircon U–Pb dating yielded an age of 156.0 ± 2.3 Ma for the BOL, and ages of 132.9 ± 1.2 and 126.2 ± 2.5 Ma for the QMLs, suggesting that they had been formed in the Late Jurassic and the Early Cretaceous, respectively.

(2) The lamprophyres originated from the partial melting of enriched lithospheric mantle that had been previously metasomatized by subduction-related fluids.

(3) The Late Jurassic lamprophyre BOL (156.0 ± 2.3 Ma) originated in the high-degree partial melting of the phlogopite-bearing lherzolite mantle in the spinel–garnet transition zone at a depth of about 60 km. One of the two Early Cretaceous QMLs (132.9 ± 1.2 Ma) was derived by the low-degree partial melting of garnet-facies lherzolite mantle at a depth of ca. 85 km. The other (126.2 ± 2.5 Ma) was produced from the low-degree partial melting of amphibole-bearing lherzolite mantle in the garnet zone at a shallower depth <85 km. Thus, from 156 to 132 Ma, the lithosphere in the study area thickened by approximately 25 km at a rate of approximately 1.0 km/Myr.

(4) The lithospheric scale of tectonic evolution, ranging from the Siberian craton *via* the Mongol–Okhotsk Suture Zone to the Songliao Block during the Kimmeridgian and the Aptian, involved three pulsed stages: the southeastward subduction of the Mongol–Okhotsk oceanic crust that resulted in the suture between the Siberian craton and the Erguna–Xing'an–Songliao Blocks in the Kimmeridgian and Tithonian, the continental collision and lithospheric thickening in the Valanginian and the Hauterivian, and the post-collisional delamination of the thickened lithosphere and its extension during the Barremian up to the Aptian.

DATA AVAILABILITY STATEMENT

The original contributions presented in the study are included in the article/supplementary material, further inquiries can be directed to the corresponding author.

AUTHOR CONTRIBUTIONS

TY: Geological context and introduction, field mapping and field relationships, geochemical and LA–ICP–MS U–Pb isotope data

processing, data documentation, petrography, discussion, and interpretations. PW: Fieldwork, geodynamic evolution model, discussion, and interpretation. YZ, YG, and CC: Fieldwork, sample collection, some petrography and data processing, parts of the analytical methods section. All authors contributed to the article and approved the submitted version.

FUNDING

This study was supported by the National Natural Science Foundation of China (NSFC No. 41790453), the National Key Research & Development Program of China (2019YFC0605402), and NSFC (Nos. 41472304, 42102129, and 41972313).

ACKNOWLEDGMENTS

We would like to thank working group of Volcanic Reservoirs and their Exploration, Jilin University, Changchun, China for their helps with field work and zircon U-Pb analyses. We also thank the two reviewers and Editors Kit Lai and Sean C. Johnson for the constructive reviews that significantly improved the manuscript.

REFERENCES

Andersen, T. (2002). Correction of Common Lead in U–Pb Analyses that Do Not Report ^{204}Pb. *Chem. Geol.* 192, 59–79. doi:10.1016/S0009-2541(02)00195-X

Choi, E., Fiorentini, M. L., Giuliani, A., Foley, S. F., Maas, R., and Taylor, W. R. (2020). Subduction-related Petrogenesis of Late Archean Calc-Alkaline Lamprophyres in the Yilgarn Craton (Western Australia). *Precambrian Res.* 338, 105550. doi:10.1016/j.precamres.2019.105550

Chung, S.-L., Chu, M.-F., Zhang, Y., Xie, Y., Lo, C.-H., Lee, T.-Y., et al. (2005). Tibetan Tectonic Evolution Inferred from Spatial and Temporal Variations in Post-collisional Magmatism. *Earth-Sci. Rev.* 68, 173–196. doi:10.1016/j.earscirev.2004.05.001

Cogné, J.-P., Kravchinsky, V. A., Halim, N., and Hankard, F. (2005). Late Jurassic-Early Cretaceous Closure of the Mongol-Okhotsk Ocean Demonstrated by New Mesozoic Paleomagnetic Results from the Trans-Baikal Area (SE Siberia). *Geophys. J. Int.* 163, 813–832. doi:10.1111/j.1365-246X.2005.02782.x

Deng, J., Liu, X., Wang, Q., Dilek, Y., and Liang, Y. (2017). Isotopic Characterization and Petrogenetic Modeling of Early Cretaceous Mafic Diking—Lithospheric Extension in the North China Craton, Eastern Asia. *GSA Bull.* 129, 1379–1407. doi:10.1130/B31609.1

Ding, L., Kapp, P., Yue, Y., and Lai, Q. (2007). Postcollisional Calc-Alkaline Lavas and Xenoliths from the Southern Qiangtang Terrane, Central Tibet. *Earth Planet. Sci. Lett.* 254, 28–38. doi:10.1016/j.epsl.2006.11.019

Duggen, S., Hoernle, K., Van Den Bogaard, P., and Garbe-schönberg, D. (2005). Post-Collisional Transition from Subduction to Intraplate-type Magmatism in the Westernmost Mediterranean: Evidence for Continental-Edge Delamination of Subcontinental Lithosphere. *J. Petrol.* 46, 1155–1201. doi:10.1093/petrology/egi013

Ellam, R. M. (1992). Lithospheric Thickness as a Control on Basalt Geochemistry. *Geology* 20, 153–156. doi:10.1130/0091-7613(1992)020<0153:ltaaco>2.3.co;2

Fitton, J. G., James, D., Kempton, P. D., Ormerod, D. S., and Leeman, W. P. (1988). The Role of Lithospheric Mantle in the Generation of Late Cenozoic Basic Magmas in the Western United States. *J. Petrol.* Special_Volume, 331–349. doi:10.1093/petrology/Special_Volume.1.331

Foley, S. F., Venturelli, G., Green, D. H., and Toscani, L. (1987). The Ultrapotassic Rocks: Characteristics, Classification, and Constraints for Petrogenetic Models. *Earth-Sci. Rev.* 24, 81–134. doi:10.1016/0012-8252(87)90001-8

Foley, S. F., Jackson, S. E., Fryer, B. J., Greenouch, J. D., and Jenner, G. A. (1996). Trace Element Partition Coefficients for Clinopyroxene and Phlogopite in an Alkaline Lamprophyre from Newfoundland by LAM-ICP-MS. *Geochim. Cosmochim. Acta* 60, 629–638. doi:10.1016/0016-7037(95)00422-X

Furman, T., and Graham, D. (1999). Erosion of Lithospheric Mantle beneath the East African Rift System: Geochemical Evidence from the Kivu Volcanic Province. *Lithos* 48, 237–262. doi:10.1016/S0024-4937(99)00031-6

Genç, Ş. C., and Tüysüz, O. (2010). Tectonic Setting of the Jurassic Bimodal Magmatism in the Sakarya Zone (Central and Western Pontides), Northern Turkey: A Geochemical and Isotopic Approach. *Lithos* 118, 95–111. doi:10.1016/j.lithos.2010.03.017

Gibson, S. A., Thompson, R. N., and Day, J. A. (2006). Timescales and Mechanisms of Plume–Lithosphere Interactions: ^{40}Ar/^{39}Ar Geochronology and Geochemistry of Alkaline Igneous Rocks from the Paraná–Etendeka Large Igneous Province. *Earth Planet. Sci. Lett.* 251, 1–17. doi:10.1016/j.epsl.2006.08.004

Guo, F., Fan, W., Wang, Y., and Zhang, M. (2004). Origin of Early Cretaceous Calc-Alkaline Lamprophyres from the Sulu Orogen in Eastern China: Implications for Enrichment Processes beneath Continental Collisional Belt. *Lithos* 78, 291–305. doi:10.1016/j.lithos.2004.05.001

Guo, F., Li, H., Fan, W., Li, J., Zhao, L., Huang, M., et al. (2015). Early Jurassic Subduction of the Paleo-Pacific Ocean in NE China: Petrologic and Geochemical Evidence from the Tumen Mafic Intrusive Complex. *Lithos* 224-225, 46–60. doi:10.1016/j.lithos.2015.02.014

Hofmann, A. W., Jochum, K. P., Seufert, M., and White, W. M. (1986). Nb and Pb in Oceanic Basalts: New Constraints on Mantle Evolution. *Earth Planet. Sci. Lett.* 79, 33–45. doi:10.1016/0012-821X(86)90038-5

Hofmann, A. W. (1997). Mantle Geochemistry: the Message from Oceanic Volcanism. *Nature* 385, 219–229. doi:10.1038/385219a0

Hoskin, P. W. O., and Schaltegger, U. (2003). The Composition of Zircon and Igneous and Metamorphic Petrogenesis. *Rev. Mineral. Geochem.* 53, 27–62. doi:10.2113/0530027

Huang, F., Zhang, Z., Xu, J., Li, X., Zeng, Y., Xu, R., et al. (2021). Lithospheric Extension in Response to Subduction of the Paleo-Pacific Plate: Insights from Early Jurassic Intraplate Volcanic Rocks in the Sk2 Borehole, Songliao Basin, NE China. *Lithos* 380-381, 105871. doi:10.1016/j.lithos.2020.105871

IJBGMR (Inner Jilin Bureau of Geology and Mineral Resources) (1977). *Report of 1:200,000 Regional Geological Research*. (Tuquan Sheet). Beijing: Geological Publishing House, 142. (in Chinese).

Ionov, D. A., Griffin, W. L., and O'Reilly, S. Y. (1997). Volatile-bearing Minerals and Lithophile Trace Elements in the Upper Mantle. *Chem. Geol.* 141, 153–184. doi:10.1016/S0009-2541(97)00061-2

Ji, Z., Meng, Q.-a., Wan, C.-b., Ge, W.-C., Yang, H., Zhang, Y.-l., et al. (2019). Early Cretaceous Adakitic Lavas and A-type Rhyolites in the Songliao Basin, NE China: Implications for the Mechanism of Lithospheric Extension. *Gondwana Res.* 71, 28–48. doi:10.1016/j.gr.2019.01.014

Ji, Z., Wan, C. B., Meng, Q. A., Zhu, D. F., Ge, W. C., Zhang, Y. L., et al. (2020). Chronostratigraphic Framework of Late Mesozoic Terrestrial Strata in the Hailar–Tamtsag Basin, Northeast China, and its Geodynamic Implication. *Geol. J.* 55, 5197–5215. doi:10.1002/gj.3731

Ji, Z., Zhang, Y.-L., Wan, C.-B., Ge, W.-C., Yang, H., Dong, Y., et al. (2021). Recycling of Crustal Materials and Implications for Lithospheric Thinning: Evidence from Mesozoic Volcanic Rocks in the Hailar-Tamtsag Basin, NE China. *Geosci. Front.* 12, 101184. doi:10.1016/j.gsf.2021.101184

Kepezhinskas, P., McDermott, F., Defant, M. J., Hochstaedter, A., Drummond, M. S., Hawkesworth, C. J., et al. (1997). Trace Element and Sr-Nd-Pb Isotopic Constraints on a Three-Component Model of Kamchatka Arc Petrogenesis. *Geochim. Cosmochim. Acta* 61, 577–600. doi:10.1016/S0016-7037(96)00349-3

Klemme, S., and O'Neill, H. S. (2000). The Near-Solidus Transition from Garnet Lherzolite to Spinel Lherzolite. *Contrib. Mineral. Petrol.* 138, 237–248. doi:10.1007/s004100050560

Labanieh, S., Chauvel, C., Germa, A., and Quidelleur, X. (2012). Martinique: a Clear Case for Sediment Melting and Slab Dehydration as a Function of Distance to the Trench. *J. Petrol.* 53, 2441–2464. doi:10.1093/petrology/egs055

Le Maitre, R. W. (2002). *Igneous Rocks: A Classification and Glossary of Terms*. second ed. Cambridge: Cambridge University Press, 236. doi:10.1017/CBO9780511535581

Li, X. H., Zhou, H. W., Wei, G. J., Liu, Y., Zhong, S. L., Luo, Q. H., et al. (2002). Geochemistry and Sr-Nd Isotopes of Cenozoic Ultrapotassic Lamprophyres in Western Yunnan: Constraints on the Composition of Sub-continental Lithospheric Mantle. *Geochimica* 31, 26–34. (in Chinese with English abstract). doi:10.19700/j.0379-1726.2002.01.005

Li, Y., Xu, W.-L., Tang, J., Pei, F.-P., Wang, F., and Sun, C.-Y. (2018). Geochronology and Geochemistry of Mesozoic Intrusive Rocks in the Xing'an Massif of NE China: Implications for the Evolution and Spatial Extent of the Mongol-Okhotsk Tectonic Regime. *Lithos* 304-307, 57–73. doi:10.1016/j.lithos.2018.02.001

Liu, Y., Gao, S., Hu, Z., Gao, C., Zong, K., and Wang, D. (2010). Continental and Oceanic Crust Recycling-Induced Melt–Peridotite Interactions in the Trans-North China Orogen: U–Pb Dating, Hf Isotopes and Trace Elements in Zircons from Mantle Xenoliths. *J. Petrol.* 51, 537–571. doi:10.1093/petrology/egp082

Liu, Y., Li, W., Feng, Z., Wen, Q., Neubauer, F., and Liang, C. (2017). A Review of the Paleozoic Tectonics in the Eastern Part of Central Asian Orogenic Belt. *Gondwana Res.* 43, 123–148. doi:10.1016/j.gr.2016.03.013

Liu, H., Li, Y., He, H., Huangfu, P., and Liu, Y. (2018). Two-phase Southward Subduction of the Mongol-Okhotsk Oceanic Plate Constrained by Permian-Jurassic Granitoids in the Erguna and Xing'an Massifs (NE China). *Lithos* 304-307, 347–361. doi:10.1016/j.lithos.2018.01.016

Lu, F. X., Zhu, Q. W., Xie, Y. H., and Zheng, J. P. (1996). Discovery of High Pressure Pyroxene Megacrystal in Dacite and Their Signficance. *Earth Sci.* 21, 541–545. (in Chinese with English abstract).

Ludwig, K. R. (2003). *ISOPLOT 3.0: A Geochronological Toolkit for Microsoft Excel*, 74. Berkeley: Berkeley Geochronology Center Special Publication.

Luo, Z. H., Wei, Y., Xin, H. T., Zhan, H. M., Ke, S., and Li, W. T. (2006). Petrogenesis of the Post-orogenic Dike Complex - Constraints to Lithosphere Delamination. *Acta Petrol. Sin.* 22, 1672–1684. (in Chinese with English abstract). doi:10.3969/j.issn.1000-0569.2006.06.024

Ma, L., Jiang, S.-Y., Hofmann, A. W., Dai, B.-Z., Hou, M.-L., Zhao, K.-D., et al. (2014). Lithospheric and Asthenospheric Sources of Lamprophyres in the Jiaodong Peninsula: A Consequence of Rapid Lithospheric Thinning beneath the North China Craton? *Geochim. Cosmochim. Acta* 124, 250–271. doi:10.1016/j.gca.2013.09.035

McKenzie, D., and Bickle, M. J. (1988). The Volume and Composition of Melt Generated by Extension of the Lithosphere. *J. Petrol.* 29, 625–679. doi:10.1093/petrology/29.3.625

McKenzie, D., and O'Nions, R. K. (1991). Partial Melt Distributions from Inversion of Rare Earth Element Concentrations. *J. Petrol.* 32, 1021–1091. doi:10.1093/petrology/32.5.1021

Menzies, M. A., Kyle, P. R., Jones, M., and Ingram, G. (1991). Enriched and Depleted Source Components for Tholeiitic and Alkaline Lavas from Zuni-Bandera, New Mexico: Inferences about Intraplate Processes and Stratified Lithosphere. *J. Geophys. Res.* 96, 13645–13671. doi:10.1029/91JB00556

Metelkin, D. V., Vernikovsky, V. A., Kazansky, A. Y., and Wingate, M. T. D. (2010). Late Mesozoic Tectonics of Central Asia Based on Paleomagnetic Evidence. *Gondwana Res.* 18, 400–419. doi:10.1016/j.gr.2009.12.008

Middlemost, E. A. K. (1994). Naming Materials in the Magma/igneous Rock System. *Earth-Sci. Rev.* 37, 215–224. doi:10.1016/0012-8252(94)90029-9

Niu, X., Chen, B., Feng, G., Liu, F., and Yang, J. (2017). Origin of Lamprophyres from the Northern Margin of the North China Craton: Implications for Mantle Metasomatism. *J. Geol. Soc.* 174, 353–364. doi:10.1144/jgs2016-044

Niu, Y. (2021). Lithosphere Thickness Controls the Extent of Mantle Melting, Depth of Melt Extraction and Basalt Compositions in All Tectonic Settings on Earth – A Review and New Perspectives. *Earth-Sci. Rev.* 217, 103614. doi:10.1016/j.earscirev.2021.103614

Ouyang, H., Mao, J., Zhou, Z., and Su, H. (2015). Late Mesozoic Metallogeny and Intracontinental Magmatism, Southern Great Xing'an Range, Northeastern China. *Gondwana Res.* 27, 1153–1172. doi:10.1016/j.gr.2014.08.010

Owen, J. P. (2008). Geochemistry of Lamprophyres from the Western Alps, Italy: Implications for the Origin of an Enriched Isotopic Component in the Italian Mantle. *Contrib. Mineral. Petrol.* 155, 341–362. doi:10.1007/s00410-007-0246-0

Pearce, J. (1983). "Role of Sub-continental Lithosphere in Magma Genesis at Destructive Plate Margins," in *Continental Basalts and Mantle Xenoliths*. Editors C. J. Hawkesworth and M. J. Norry (Nantwich: Shiva Publishing), 158–185.

Peccerillo, A., and Taylor, S. R. (1976). Geochemistry of Eocene Calc-Alkaline Volcanic Rocks from the Kastamonu Area, Northern Turkey. *Contr. Mineral. Petrol.* 58, 63–81. doi:10.1007/BF00384745

Plank, T., and Langmuir, C. H. (1998). The Chemical Composition of Subducting Sediment and its Consequences for the Crust and Mantle. *Chem. Geol.* 145, 325–394. doi:10.1016/S0009-2541(97)00150-2

Polat, A., and Hofmann, A. W. (2003). Alteration and Geochemical Patterns in the 3.7–3.8 Ga Isua Greenstone Belt, West Greenland. *Precambrian Res.* 126, 197–218. doi:10.1016/S0301-9268(03)00095-0

Rapp, R. P., and Watson, E. B. (1995). Dehydration Melting of Metabasalt at 8–32 Kbar: Implications for Continental Growth and Crust-Mantle Recycling. *J. Petrol.* 36, 891–931. doi:10.1093/petrology/36.4.891

Robinson, J. A. C., and Wood, B. J. (1998). The Depth of the Spinel to Garnet Transition at the Peridotite Solidus. *Earth Planet. Sci. Lett.* 164, 277–284. doi:10.1016/S0012-821X(98)00213-1

Rocchi, S., Di Vincenzo, G., Ghezzo, C., and Nardini, I. (2009). Granite-amprophyre Connection in the Latest Stages of the Early Paleozoic Ross Orogeny (Victoria Land, Antarctica). *Geol. Soc. Am. Bull.* 121, 801–819. doi:10.1130/B26342.1

Rock, N. M. S., and Groves, D. I. (1988). Can Lamprophyres Resolve the Genetic Controversy over Mesothermal Gold Deposits? *Geology* 16, 538–541. doi:10.1130/0091-7613(1988)016<0538:clrtgc>2.3.co;2

Rock, N. M. S. (1987). "The Nature and Origin of Lamprophyres: an Overview," in *Alkaline Igneous Rocks*. Editors J. G. Fitton and B. G. J. Upton (London: Geological Society Special Publications), 30, 191–226. doi:10.1144/gsl.sp.1987.030.01.09

Rock, N. M. S. (1991). *Lamprophyres*. London: Blackie, 225.

Rudnick, R. L., and Gao, S. (2003). "Composition of the Continental Crust," in *Treatise on Geochemistry*. Editors H. D. Holland and K. K. Turekian (Oxford: Pergamon), 1–64. doi:10.1016/b0-08-043751-6/03016-4

Rudnick, R. L., Gao, S., Ling, W.-l., Liu, Y.-s., and McDonough, W. F. (2004). Petrology and Geochemistry of Spinel Peridotite Xenoliths from Hannuoba and Qixia, North China Craton. *Lithos* 77, 609–637. doi:10.1016/j.lithos.2004.03.033

Secher, K., Heaman, L. M., Nielsen, T. F. D., Jensen, S. M., Schjøth, F., and Creaser, R. A. (2009). Timing of Kimberlite, Carbonatite, and Ultramafic Lamprophyre Emplacement in the Alkaline Province Located 64°–67° N in Southern West Greenland. *Lithos* 112, 400–406. doi:10.1016/j.lithos.2009.04.035

Soder, C. G., and Romer, R. L. (2018). Post-Collisional Potassic–Ultrapotassic Magmatism of the Variscan Orogen: Implications for Mantle Metasomatism during Continental Cubduction. *J. Petrol.* 59, 1007–1034. doi:10.1093/petrology/egy053

Stille, P., Oberhänsli, R., and Wenger-Schenk, K. (1989). Hf-Nd Isotopic and Trace Element Constraints on the Genesis of Alkaline and Calc-Alkaline Lamprophyres. *Earth Planet. Sci. Lett.* 96, 209–219. doi:10.1016/0012-821X(89)90133-7

Su, Y., Zheng, J., Griffin, W. L., Zhao, J., Tang, H., Ma, Q., et al. (2012). Geochemistry and Geochronology of Carboniferous Volcanic Rocks in the Eastern Junggar Terrane, NW China: Implication for a Tectonic Transition. *Gondwana Res.* 22, 1009–1029. doi:10.1016/j.gr.2012.01.004

Sun, S.-s., and McDonough, W. F. (1989). "Chemical and Isotopic Systematics of Oceanic Basalts: Implications for Mantle Composition and Processes," in *Magmatism Ocean Basins*. Editors A. D. Saunders and M. J. Norry (London: Special Publications), 42, 313–345. doi:10.1144/gsl.sp.1989.042.01.19

Tang, J., Xu, W.-L., Wang, F., Zhao, S., and Li, Y. (2015). Geochronology, Geochemistry, and Deformation History of Late Jurassic–Early Cretaceous Intrusive Rocks in the Erguna Massif, NE China: Constraints on the Late Mesozoic Tectonic Evolution of the Mongol-Okhotsk Orogenic Belt. *Tectonophysics* 658, 91–110. doi:10.1016/j.tecto.2015.07.012

Tarney, J., and Jones, C. E. (1994). Trace Element Geochemistry of Orogenic Igneous Rocks and Crustal Growth Models. *J. Geol. Soc.* 151, 855–868. doi:10.1144/gsjgs.151.5.0855

Taylor, S. R., and McLennan, S. M. (1985). *The Continental Crust: Its Composition and Evolution*. Oxford: Blackwell Scientific, 312.

Thirlwall, M. F., Smith, T. E., Graham, A. M., Theodorou, N., Hollings, P., Davidson, J. P., et al. (1994). High Field Strength Element Anomalies in Arc Lavas: Source or Process? *J. Petrol.* 35, 819–838. doi:10.1093/petrology/35.3.819

Thompson, R. N., and Morrison, M. A. (1988). Asthenospheric and Lower-Lithospheric Mantle Contributions to Continental Extensional Magmatism:

An Example from the British Tertiary Province. *Chem. Geol.* 68, 1–15. doi:10.1016/0009-2541(88)90082-4

van der Meer, Q. H. A., Storey, M., Scott, J. M., and Waight, T. E. (2016). Abrupt Spatial and Geochemical Changes in Lamprophyre Magmatism Related to Gondwana Fragmentation Prior, during and after Opening of the Tasman Sea. *Gondwana Res.* 36, 142–156. doi:10.1016/j.gr.2016.04.004

Wang, F., Zhou, X.-H., Zhang, L.-C., Ying, J.-F., Zhang, Y.-T., Wu, F.-Y., et al. (2006). Late Mesozoic Volcanism in the Great Xing'an Range (NE China): Timing and Implications for the Dynamic Setting of NE Asia. *Earth Planet. Sci. Lett.* 251, 179–198. doi:10.1016/j.epsl.2006.09.007

Wang, P. J., Gao, Y. F., Ren, Y. G., Liu, W. Z., and Zhang, J. G. (2009). $^{40}Ar/^{39}Ar$ Age and Geochemical Features of Mugearite from the Qingshankou Formation; Significances for Basin Formation, Hydrocarbon Generation and Petroleum Accumulation of the Songliao Basin in Cretaceous. *Acta Petrol. Sin.* 25, 1178–1190. (in Chinese with English abstract).

Wang, W., Tang, J., Xu, W.-L., and Wang, F. (2015). Geochronology and Geochemistry of Early Jurassic Volcanic Rocks in the Erguna Massif, Northeast China: Petrogenesis and Implications for the Tectonic Evolution of the Mongol–Okhotsk Suture Belt. *Lithos* 218-219, 73–86. doi:10.1016/j.lithos.2015.01.012

Wang, P.-J., Mattern, F., Didenko, N. A., Zhu, D.-F., Singer, B., and Sun, X.-M. (2016). Tectonics and Cycle System of the Cretaceous Songliao Basin: An Inverted Active Continental Margin Basin. *Earth-Sci. Rev.* 159, 82–102. doi:10.1016/j.earscirev.2016.05.004

Wang, F., Xu, W. L., Xing, K. C., Wang, Y. N., Zhang, H. H., Wu, W., et al. (2019). Final Closure of the Paleo-Asian Ocean and Onset of Subduction of Paleo-Pacific Ocean: Constraints from Early Mesozoic Magmatism in Central Southern Jilin Province, NE China. *J. Geophys. Res. Solid Earth* 124, 2601–2622. doi:10.1029/2018JB016709

Woolley, A. R., Bergman, S. C., Edgar, A. D., Le Bas, M. J., Mitchell, R. H., Rock, N. M. S., et al. (1996). Classification of Lamprophyres, Lamproites, Kimberlites, and the Kalsilitic, Melilitic, and Leucitic Rocks. *Can. Mineral.* 34, 175–186.

Wu, F.-Y., Sun, D.-Y., Ge, W.-C., Zhang, Y.-B., Grant, M. L., Wilde, S. A., et al. (2011). Geochronology of the Phanerozoic Granitoids in Northeastern China. *J. Asian Earth Sci.* 41, 1–30. doi:10.1016/j.jseaes.2010.11.014

Wyman, D. A., Ayer, J. A., Conceição, R. V., and Sage, R. P. (2006). Mantle Processes in an Archean Orogen: Evidence from 2.67 Ga Diamond-Bearing Lamprophyres and Xenoliths. *Lithos* 89, 300–328. doi:10.1016/j.lithos.2005.12.005

Xu, W. L., Sun, D. Y., and Zhou, Y. (1994). *Manzhouli-Suifenhe Geoscience Transect Magmatism and Crust Structure*. Beijing: Geological Publishing House, 94. (in Chinese).

Xu, W.-L., Pei, F.-P., Wang, F., Meng, E., Ji, W.-Q., Yang, D.-B., et al. (2013). Spatial-temporal Relationships of Mesozoic Volcanic Rocks in NE China: Constraints on Tectonic Overprinting and Transformations between Multiple Tectonic Regimes. *J. Asian Earth Sci.* 74, 167–193. doi:10.1016/j.jseaes.2013.04.003

Yang, B. J., Mu, S. M., Jin, X., and Liu, C. (1996). Synthesized Study on the Geophysics of Manzhouli-Suifenhe Geoscience Transect, China. *Acta geophys. Sin.* 39, 772–782. (in Chinese with English abstract).

Yuan, H., Gao, S., Liu, X., Li, H., Günther, D., and Wu, F. (2004). Accurate U-Pb Age and Trace Element Determinations of Zircon by Laser Ablation-Inductively Coupled Plasma-Mass Spectrometry. *Geostand. Geoanalyt Res.* 28, 353–370. doi:10.1111/j.1751-908X.2004.tb00755.x

Zhang, H. H., Xu, Y. G., Ge, W. C., and Ma, J. L. (2006). Geochemistry of Late Mesozoic-Cenozoic Basalts in Yitong-Datun Area, Jilin Province and its Implication. *Acta Petrol. Sin.* 22, 1579–1596. (in Chinese with English abstract).

Zhang, J.-H., Gao, S., Ge, W.-C., Wu, F.-Y., Yang, J.-H., Wilde, S. A., et al. (2010). Geochronology of the Mesozoic Volcanic Rocks in the Great Xing'an Range, Northeastern China: Implications for Subduction-Induced Delamination. *Chem. Geol.* 276, 144–165. doi:10.1016/j.chemgeo.2010.05.013

Zhang, F. Q., Chen, H. L., Yu, X., Dong, C. W., Yang, S. F., Pang, Y. M., et al. (2011). Early Cretaceous Volcanism in the Northern Songliao Basin, NE China, and its Geodynamic Implication. *Gondwana Res.* 19, 163–176. doi:10.1016/j.gr.2010.03.011

Zhang, C., Quan, J.-Y., Zhang, Y.-J., Liu, Z.-H., Li, W., Wang, Y., et al. (2020). Late Mesozoic Tectonic Evolution of the Southern Great Xing'an Range, NE China: Evidence from Whole-Rock Geochemistry, and Zircon U-Pb Ages and Hf Isotopes from Volcanic Rocks. *Lithos* 362-363, 105409. doi:10.1016/j.lithos.2020.105409

Zhou, X. H. (2006). Major Transformation of Subcontinental Lithosphere beneath Eastern China in the Cenozoic-Mesozoic: Review and Prospect. *Earth Sci. Front.* 13, 50–64. (in Chinese with English abstract).

Conflict of Interest: The authors declare that the research was conducted in the absence of any commercial or financial relationships that could be construed as a potential conflict of interest.

Publisher's Note: All claims expressed in this article are solely those of the authors and do not necessarily represent those of their affiliated organizations, or those of the publisher, the editors and the reviewers. Any product that may be evaluated in this article, or claim that may be made by its manufacturer, is not guaranteed or endorsed by the publisher.